The Repeating Major Earthquakes in the Mexican Subduction Zone Along Oaxaca: Implications for Future Events

Ricardo Garza-Giron*1,2,0, Thorne Lay^{2,0}, and Lingling Ye^{3,0}

Abstract

The subduction zone along Oaxaca, Mexico, has experienced multiple $M_{\rm w} \geq 7$ earth-quakes that ruptured in close proximity several decades apart in at least three locations along the coast. Similarity of waveform recordings from a few long-period seismic stations at teleseismic distances has provided evidence for up to three repeated failures of the same slip patches, or persistent asperities, in the region. The evidence from prior single-station comparisons is bolstered by considering azimuthally distributed sets of body-wave recording pairs for the 1968 and 2018 Pinotepa Nacional (western Oaxaca), and 1965 and 2020 La Crucecita (eastern Oaxaca) earthquakes, as viewed in the long-period World-Wide Standardized Seismograph Network instrument passband (> 5 s period). Drawing on detailed slip inversions for the most recent events and observations of their relationships with regional slow-slip events, we note features to be alert for in central Oaxaca where prior repeating events in 1928 and 1978 occurred and there is potential for a similar future event.

Cite this article as Garza-Giron, R., T. Lay, and L. Ye (2024). The Repeating Major Earthquakes in the Mexican Subduction Zone Along Oaxaca: Implications for Future Events, *Seismol. Res. Lett.* XX, 1–13, doi: 10.1785/0220240267.

Supplemental Material

Introduction

The coastal region of the state of Oaxaca, Mexico, has experienced over a dozen seismically recorded major earthquakes ($M \geq 7$) during the last 120 yr (Fig. 1). The 16 February 2018 Pinotepa Nacional ($M_{\rm w}$ 7.2) and 23 June 2020 La Crucecita ($M_{\rm w}$ 7.4) events are the most recent in the region. Servicio Sismológico Nacional (SSN) reported that these two earthquakes caused significant damage in local communities and were felt in Mexico City, approximately 450 km away. Prior, comparable-size, damaging earthquakes struck near Pinotepa in 1928 and 1968, near La Crucecita in 1928 and 1965, and the intervening region of central Oaxaca was struck in 1928 twice and in 1978 (Fig. 1).

Given their relatively short interevent times of \sim 45 yr and their destructive power; earthquakes along the Oaxaca subduction zone present a high-seismic risk. It is striking that four major events struck along the coast in 1928 over a period of seven months, on 4 August, 9 October, 17 June, and 22 March, spanning from west offshore Pinotepa Nacional to east near La Crucecita (Singh *et al.*, 1981, 1984; Santoyo *et al.*, 2005). A great ($M_{\rm w} \sim$ 8.6) earthquake in 1787 appears to have ruptured the entire shallow portion of the megathrust from western to eastern Oaxaca (Suárez and Albini, 2009), spanning the 1928 sequence, suggesting that the southern Mexican subduction zone can intermittently host a great event when stress loading and triggering conditions are favorable, but will more commonly rupture in multiple smaller events. Such zone-spanning

events have also occurred along Sumatra (Lay *et al.*, 2005), Colombia (Kanamori and McNally, 1982; Ye *et al.*, 2016), and Honshu (Lay, 2018). Understanding the characteristics of the more typical ruptures is important for assessing the seismic hazard in the region.

The largest earthquake in the last 120 yr in Oaxaca was the 1907 ($M_{\rm s}$ 8) earthquake, which has uncertain location, being placed by some catalogs in central Oaxaca (Fig. 1) or in the vicinity of the border of Oaxaca and Guerrero near subsequent ruptures in 1937 $M_{\rm s}$ 7.4, 1950 $M_{\rm s}$ < 7.1, and 1957 $M_{\rm s}$ 7.7 (Nishenko and Singh, 1987). Further west from Pinotepa Nacional, the 2012 $M_{\rm s}$ 7.4 Ometepec earthquake (U.N.A de Mexico Seismology, 2013; Graham *et al.*, 2014) ruptured the same area as a 1982 doublet ($M_{\rm s}$ 6.9 and 7.0) and at least three other prior earthquakes (1890 $M_{\rm s}$ 7.3, 1937 $M_{\rm s}$ 7.5, and 1950 $M_{\rm s}$ 7.3) (Astiz and Kanamori, 1984). Sequential ruptures of similar size in approximately the same area, with relatively short interevent times, are common along Mexico, providing

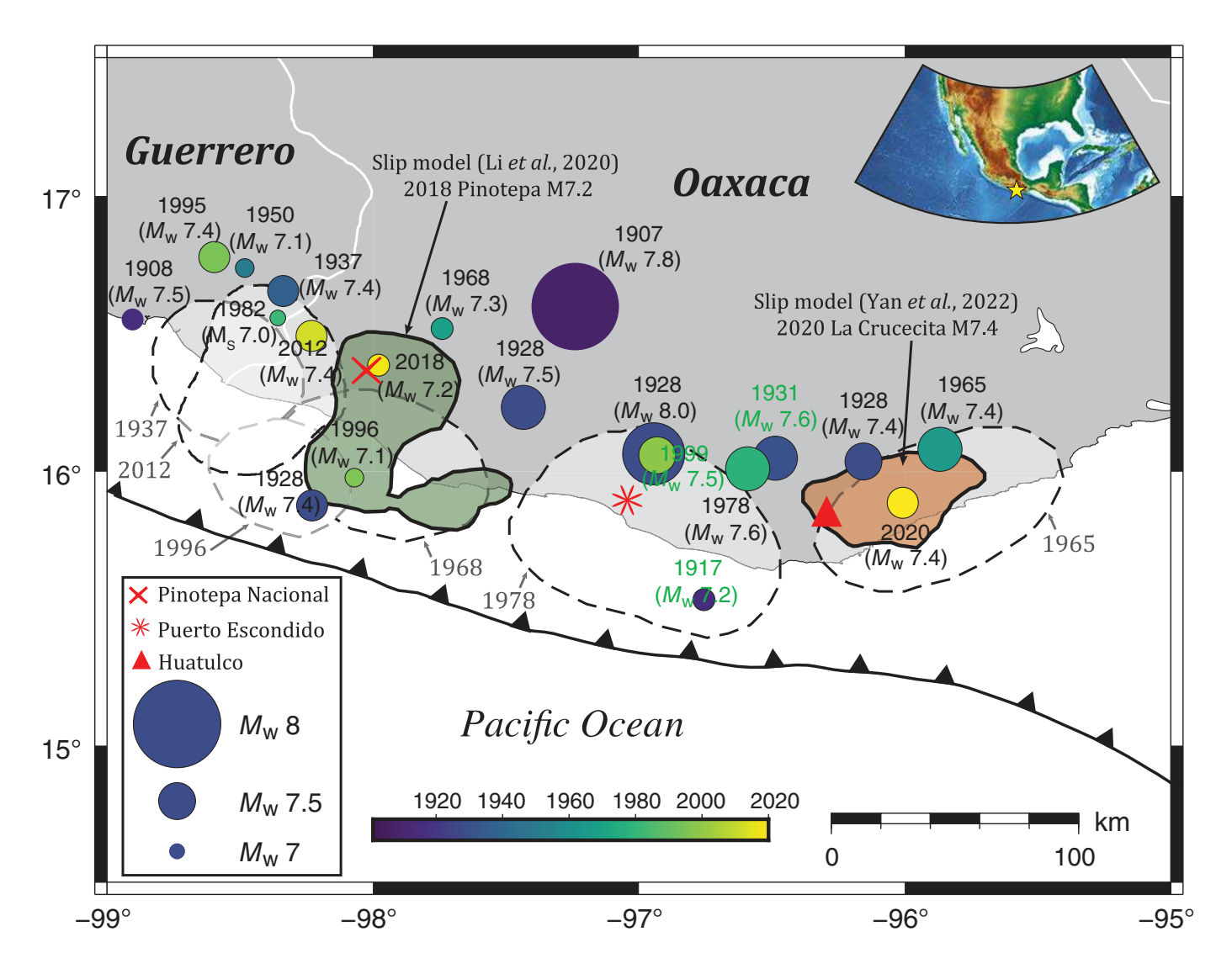
^{1.} Department of Geosciences, Warner College of Natural Resources, Colorado State University, Fort Collins, Colorado, U.S.A., https://orcid.org/0000-0001-9775-9635 (RG-G); 2. Department of Earth and Planetary Sciences, University of California, Santa Cruz, California, U.S.A., https://orcid.org/0000-0003-2360-4213 (TL);

^{3.} Department of Earth and Space Sciences, Southern University of Science and Technology, Shenzhen, China,

https://orcid.org/0000-0001-9689-4149 (LY)

^{*}Corresponding author: rickygg@colostate.edu

[©] Seismological Society of America



many of the limited examples of complete seismologically recorded major earthquake cycles around the Pacific.

Teleseismic seismograms have demonstrated that most observed major events along Mexico involve relatively simple ruptures that produce similar body waveforms at individual long-period stations in directions of stable *P*-wave radiation pattern (e.g., Chael and Stewart, 1982; Astiz and Kanamori, 1984; Astiz *et al.*, 1987; Singh and Mortera, 1991; Hjörleifsdóttir *et al.*, 2016). This suggests that discrete localized locked patches (asperities) tend to rupture in this subduction zone (Ye *et al.*, 2018).

Recently, Singh *et al.* (2023) tested the hypothesis that nearby major events along the Mexican subduction zone are repeating events that rupture precisely the same portion of the plate boundary, based on comparing teleseismic long-period seismograms recorded at one or two stations operating with Galitzin instruments. They proposed, based on similarity of pairs of long-duration seismic recordings and assuming the instrument responses have been sufficiently stable, that for western Oaxaca, where the 2018 Pinotepa earthquake occurred, there have been at least three repeaters (1928, 1968, and 2018); Suárez *et al.* (2020) suggested that this region probably also ruptured in 1854 and 1890,

Figure 1. Large earthquakes along the Oaxaca subduction zone. Earthquake hypocenters with $M \ge 7.0$ in the last 120 yr are shown by circles, scaled by $M_0/8 \times 10^{20}$, and colored by time since 1900. The rupture zones of large historic earthquakes inferred from the distribution of aftershocks are indicated with the light dashed line polygons. The finite-fault slip area for the 2018 $M_{\rm w}$ 7.2 Pinotepa earthquake (Li et al., 2020) is shown with green shading, and the finite-fault slip area for the 2020 $M_{\rm w}$ 7.4 La Crucecita earthquake (Yan et al., 2022) is plotted using orange shading. Large earthquakes on 9 October 1928 and 22 March 1928 ruptured in the Pinotepa and La Crucecita regions, respectively. The large 17 June 1928 $M_{\rm w}$ 8.0 earthquake ruptured in the same central Oaxaca region as the 1978 $M_{\rm w}$ 7.6 ($M_{\rm s}$ 7.8) earthquake. The 1907 earthquake has large location uncertainty, and some catalogs place it in Guerrero. Red symbols represent the location of the most populated cities in the region. Top right inset shows the regional location of the Oaxaca Subduction Zone.

prior to availability of well-calibrated seismic recordings. For eastern Oaxaca, where the 2020 La Crucecita earthquake ruptured, similarity of pairs of waveforms suggest that there have also been three repeaters (1928, 1965, and 2020) (Singh *et al.*,

2023), and this same area probably ruptured previously in 1801 and 1870 (Suárez et al., 2020). Singh et al. (2023) also document that for the region of central Oaxaca there has been one repeating pair (17 June 1928 and 29 November 1978; Fig. 1).

The fact that similar waveforms at a given station can be observed for well-separated events raises concern about designating events as repeaters using only similarity of short intervals of a pair of long-period recordings. For example, Liu *et al.* (2023) demonstrate that the 2022 Coalcomán, Michoacán, earthquake ruptured an overlapping, but not identical source area as the prior 1973 Michoacán earthquake based on azimuthal waveform variations. Singh *et al.* (2023) reduced this concern using long seismogram segments at individual stations that capture bodyand surface-wave signals, with the latter decorrelating markedly for shifts in slip centroid locations exceeding ~30 km, comparable to the scale of the inferred asperities.

Here, we expand on the event comparisons of Singh et al. (2023) by comparing azimuthally distributed body-wave seismograms for two sets of $M_{\rm w} > 7$ earthquakes: the 2 August 1968 $M_{\rm s}$ 7.1 and 2018 $M_{\rm w}$ 7.2 Pinotepa Nacional earthquakes and the 23 August 1965 $M_{\rm s}$ 7.6 and 2020 $M_{\rm w}$ 7.4 La Crucecita earthquakes. Analog recordings from the World-Wide Standardized Seismograph Network (WWSSN) for the 1965 and 1968 events were obtained from the archive at the Earthquake Research Institute of the University of Tokyo (Satake et al., 2020). Although long-duration recordings are not available due to surface waves going offscale on the long-period seismic records for the early events in each comparison, numerous onscale body-wave intervals of variable duration could be digitized spanning a wide range of azimuths that sample the P, PP, and sometimes, PPP wave radiation pattern broadly. This allows for the evaluation of azimuthal waveform similarity for periods greater than 5 s. The waveform comparisons strengthen assessments of whether the southern Mexican subduction zone can be represented by a simple wellseparated persistent asperity model with low-triggering interaction that gives rise to relatively consistent earthquake cycles and only intermittent synchronization into great earthquakes (e.g., Lay and Kanamori, 1981). Assessing the extent to which these Oaxaca events are true repeaters also provides insights into the slip history and future of the area and the implications for the degree of heterogeneity on the plate boundary, which are governing factors for understanding the nucleation process of major earthquakes and their possible recurrence time.

Data and Methods

At the time that the 1965 and 1968 earthquakes occurred in Mexico, the WWSSN was operating over 100 stations around the world, with stable instrument performance. The WWSSN was deployed in the early 1960s by the U.S. Coast and Geodetic Survey (Oliver and Murphy, 1971). Each station operated three-component short-period Benioff seismometers (Benioff, 1955) and three-component long-period Sprengnether

Press-Ewing Instruments (Press *et al.*, 1958). By 1965 most of the long-period seismometers operated with a 15 s period pendulum response (Peterson and Hutt, 2014). The ground motions were recorded on photographic paper on rotating drums, producing daily records with minute tick marks spaced by 15 or 30 mm depending on the rotation rate of the drum. After onsite photo development, the paper records were copied to 70 or 35 mm film. Typically, portions of the film would be printed onto paper for analysis or manual digitization.

We use scanned images of long-period vertical-component body waves from 35 mm film reels for WWSSN stations for the 1965 and 1968 earthquakes in the repository of the Earthquake Research Institute at the University of Tokyo. The waveforms are digitized using the ImageJ software package (Schneider et al., 2012). For each WWSSN record image, we establish the time and amplitude scales by measuring the minute-long intervals between time tick-marks for each station (Fig. 2). The waveforms are vectorized by detrending the digitized data and interpolating to have a sampling rate of 1 sample per second. The signal is then band-pass filtered in a band from 100 to 5 s with an acausal (two-pass) Butterworth filter. For each useful WWSSN recording, we search for a collocated, contemporary broadband station recording of either the 2018 Pinotepa or 2020 La Crucecita earthquakes. In the absence of a collocated station, we search for the nearest station within a 1000 km distance (most station pairs are much closer). We use a generous distance latitude to ensure good coverage of station pairs for short seismogram time intervals and to establish the reduction in correlation expected for longer time intervals as station separation increases. This provides a total of 34 pairs of recordings for the 1968 and 2018 earthquakes (Table S1, Figs. S1, S2, available in the supplemental material to this article) and 13 pairs for the 1965 and 2020 earthquakes (Table S2, Figs. S1, S3).

Processing of broadband data involves demeaning and detrending the signals and applying a 10% Hanning taper to each end of the trace. We deconvolve the records to displacement by removing the instrument response and applying a prefilter with corner frequencies at 100, 20, 2, and 1 s to stabilize the deconvolution. The signals are then convolved with the instrument response of the WWSSN long-period stations (Peterson and Hutt, 2014). We filter the data with the same filter used for the WWSSN data (two-pass band-pass Butterworth filter between 100 and 5 s) and apply an amplitude correction corresponding to the magnification of the WWSSN record at each station. For example, the magnification for the record at station SBA (Scott Base, Antarctica) is 750 (see Fig. 2a, inset). The magnification factors used for each station are listed in Tables S1 and S2.

To assess similarity between earlier and recent event recordings, and to establish significance relative to comparisons with other large earthquakes in Oaxaca, we compute time-domain normalized cross-correlation coefficients using time windows of 150 s of data straddling the *P*-wave arrival (10 s before to

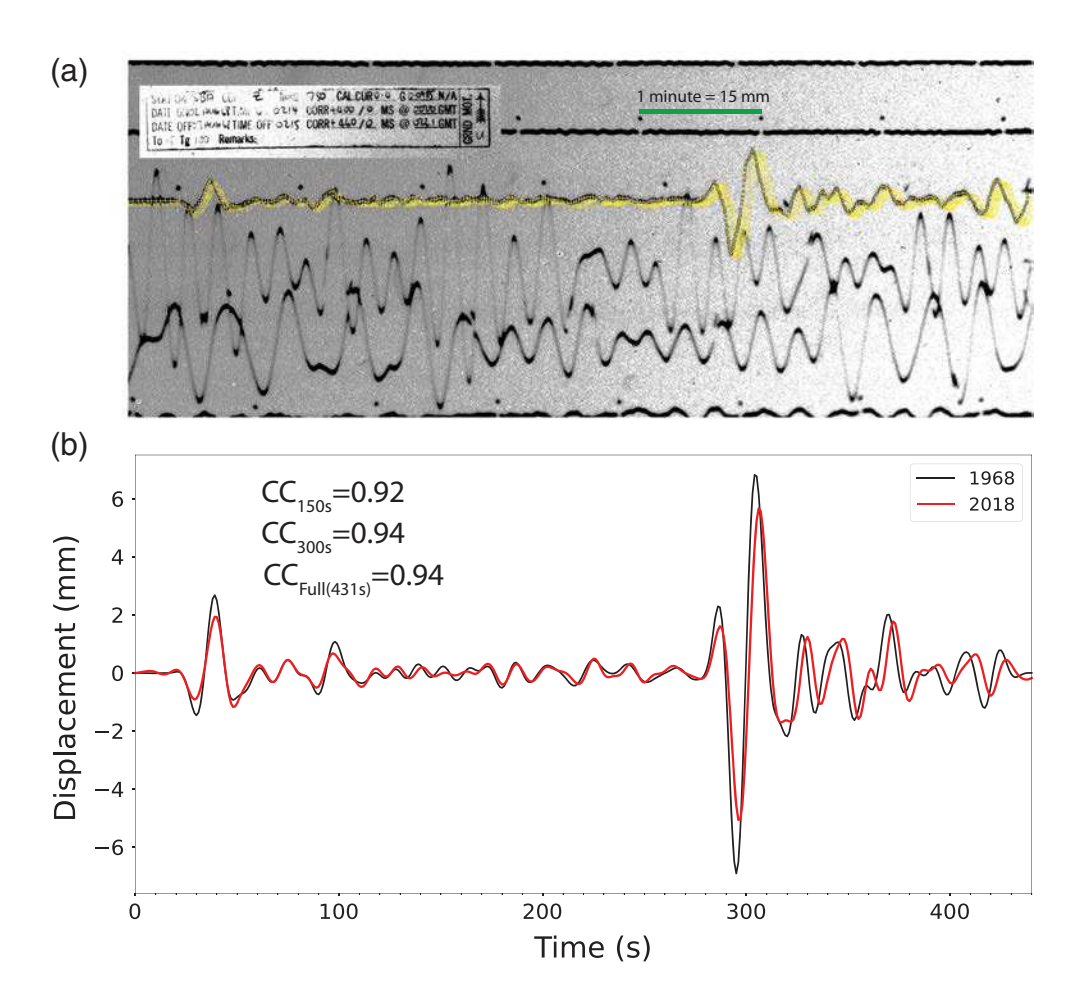


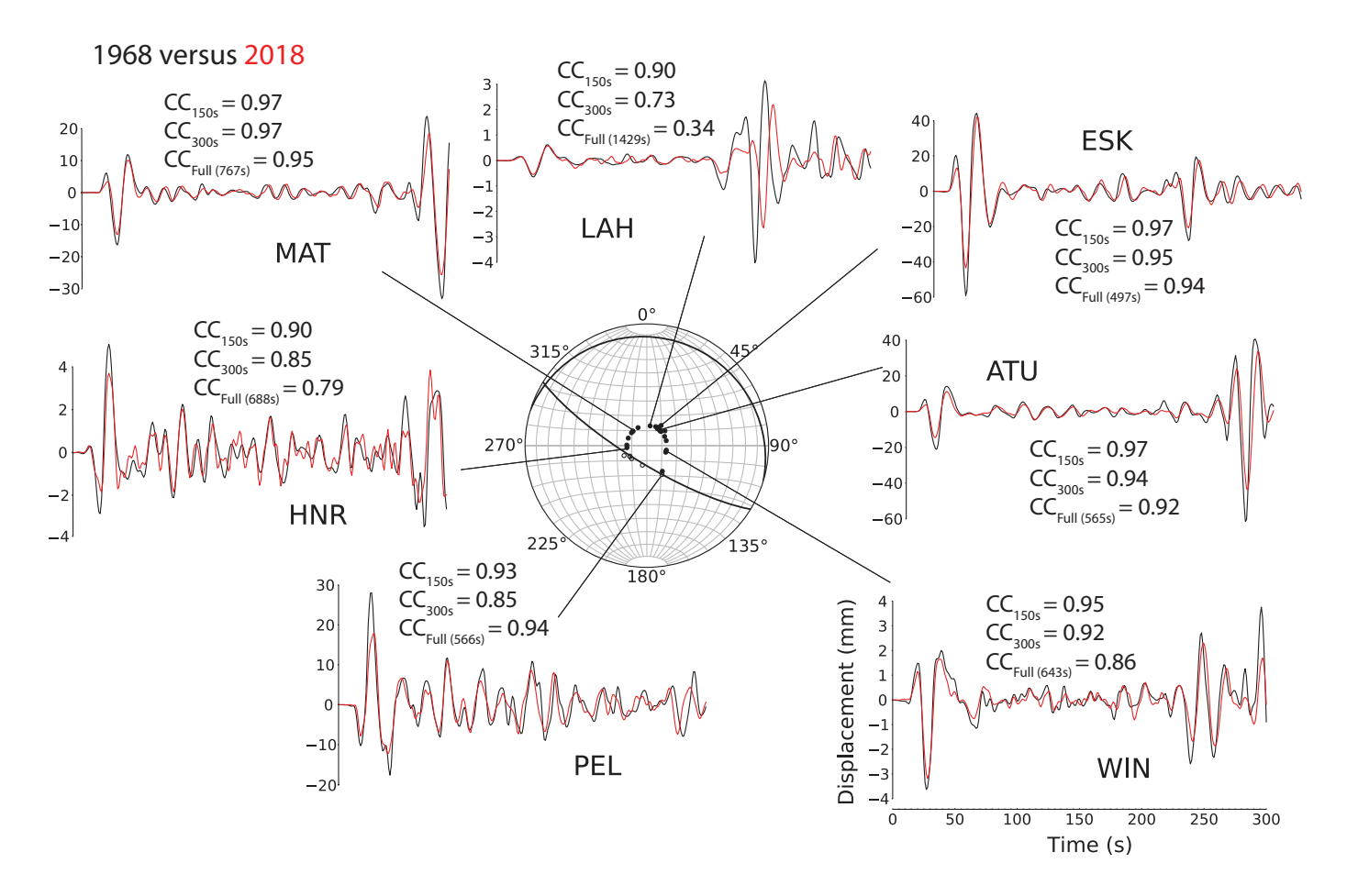
Figure 2. Example of waveform digitization and comparison. (a) Scanned image of the film record and digitized data points (yellow) for the 23 August 1968 event recorded at World-Wide Standardized Seismograph Network (WWSSN) station Scott Base, Antarctica (SBA). The inset displays the information on the paper record label, and the green line shows the time–distance scaling factor. (b) Waveform comparison between the 1968 event (black) and the 16 February 2018 event (red) recorded at SBA. The records of all stations used for the 2018 and 2020 events are deconvolved to displacement, convolved with the nominal response of the 15 s long-period WWSSN instrument, and filtered in the passband of 5–100 s. The digitized WWSSN records are vectorized by detrending, interpolating to an evenly spaced time series, and filtering with the same passband filter as the contemporary records. The amplitudes of all the WWSSN records are equalized using the magnification value of each station. Normalized cross-correlation coefficients for the first 150 and 300 s of the record as well as for the entire digitized record are shown.

140 s after, CC_{150s}) and 300 s (10 s before *P*-wave arrival and 290 s after, CC_{300s}), and also using the full extent of the digitized traces, CC_{Full} , which vary in length, but typically exceed 300 s. An exception is made for stations with less than 150 s of digitized trace to be included in the analysis. For the 2018 and 1968 events comparison, we include stations ADE (Adelaide, Australia), JER (Jerusalem), and MUN (Mundaring, Australia), and for the 2020 and 1965 events comparison we include stations KEV (Kevo, Finland), SJG (San Juan, Puerto Rico), and SOM (Sombrero, Chile), all with total lengths below 150 s (see Tables S1 and S2). In those cases, the 150 s window cross correlation was performed by minor padding of the signals with zeros. The choice of the windows aims at comparing traces including different phase

arrivals, and therefore increasthe sensitivity between waveform pairs in terms of potential source offsets. However, we acknowledge that by choosing discrete windows, our analysis is susceptible to inherent imperfections in the paper record digitization, which can be present at different times throughout the trace, and thus it can cause a local degradation of the cross correlation. address this issue by analyzing maximum cross-correlation coefficients as a continuous function of window size, which range from 100 s to the maximum length of the digitized trace at each station in 5 s increments.

Although the data processing is straightforward and robust for broadband digital recordings, various errors may be incurred in digitizing and vectorizing WWSSN recordings. Some distortion of the photographic images results from irregularity in the drum rotation rate, original flatness of the photographic paper on the rotating drum, blurriness in the light trace from the galvanometer mirror and the photo development, distortion in the filming of the original record, and error in the image digitization. Although filtering of the digitized and vectorized

signal addresses most of these issues, timing irregularity along the trace can only be corrected approximately based on variation in time between minute marks on adjacent rows of the recordings (e.g., Dost and Haak, 2006). To evaluate such an approach, we tested minute-to-minute stretching on collocated stations, which show modest phase lags in different sections of the record (e.g., stations ESK and ATU for the 1968 and 2018 events). Our tests revealed that the minute-by-minute corrections did not enhance the significance of the maximum cross-correlations. As a result, we opted to calibrate the digitized window length using multiple-minute marks, which effectively average out such differences across the entire time window (which is less than 12 min long in most cases). Our results demonstrate significant



outcomes even with this minor averaging process. Errors in the instrument magnification and frequency response over time are also hard to account for, with the daily calibration pulse shape and amplitude being the primary guide on individual instrument stability. We restrict our analysis to seismograms with relatively stable calibration pulses, but some gain errors are likely.

Results

The 1968 M_s 7.1 and 2018 M_w 7.2 Pinotepa events

The relatively abundant WWSSN records of the 1968 Pinotepa earthquake that were adequate for digitization provide numerous comparisons with the 2018 Pinotepa earthquake to further test whether these events are repeaters or not. A subset of the total number of seismogram pairs for the 1968 and 2018 Pinotepa events, corrected to WWSSN instrumental displacement amplitude units, along with first-motion polarities projected onto a lower focal hemisphere, are shown in Figure 3. All additional waveform comparisons are shown in Figure S2 and details on the station locations, epicentral distances, distance between stations if not collocated, and cross-correlation values for the first 150 s of data as well as cross-correlation values for 300 s windows and the full length of the digitized traces are shown in Table S1. Station ESK (Eskdalemuir, Scotland) has frequently been used to consider complexity of signals from Mexican megathrust earthquakes (e.g., Chael and Stewart,

Figure 3. Examples of waveform comparisons for the 2 August 1968 M_s 7.1 Pinotepa event (black traces) and the 16 February 2018 $M_{\rm w}$ 7.2 Pinotepa event (red traces), showing 300 s of bodywave arrivals for selected stations. The compressional P-wave first motions of all the station pairs and the *P*-wave nodal plane solution for the 1968 event from Chael and Stewart (1982) is shown on an equal-area projection of the lower focal hemisphere. Waveform pairs are shown with WWSSN instrument response displacement amplitudes. Normalized cross-correlation coefficients using 150 and 300 s of waveform, as well as the full extent of the digitized traces, are shown for each station. Additional waveform comparisons are shown in Figure S2. The high-waveform shape cross-correlations for >5 s periods and the good azimuthal coverage of stations demonstrate that the 1968 and 2018 events can be characterized as truly repeated ruptures of the same megathrust area.

1982; Astiz and Kanamori, 1984) because the ray paths to this station sample a stable part of the P-wave radiation pattern (Fig. 3). The similarity of the equalized ESK waveforms for periods greater than 5 s for the two events is very pronounced, with normalized correlation coefficients of $CC_{150s} = 0.97$, $CC_{300s} = 0.95$, and $CC_{Full497s} = 0.94$, with the latter window spanning the P, PP, and PPP arrivals. The 2018 event P waves average about 15% lower amplitude than for the 1968 event. Singh $et\ al.\ (2023)$ observed a lower correlation of the vertical-component body waves for Galitzin response seismograms

at station STR (Strasbourg, France), but very similar surfacewave recordings for this event pair. Overall, the seismogram comparisons establish that the 2018 Pinotepa event is comparable in complexity to the other Mexican earthquakes along the trench, and particularly similar to the 1968 event.

The azimuthal coverage of the seismogram pairs for the Pinotepa events is very good, allowing a deeper evaluation of the similarities of the two events. Stations near radiation nodes are especially sensitive to differences in source location and faulting mechanism, and the high CC_{150s} at HNR (Honiara, Solomon Islands; 0.90) and PEL (Peldehue, Chile; 0.93) strongly suggest collocation of the source areas and similar mechanisms for the two events. Large CC_{150s} exceeding 0.9 are observed at other azimuths as well, with only a few traces having significantly lower CC_{Full} values such as BAG (Baguio, Philippines), MSH (Mashhad, Iran), and SHI (Shiraz, Iran), for which the PPP phase may differ and differences in station location might have a larger impact due to complex ray paths. The maximum CC_{150s} value found is 0.98 for stations AAE (Addis Ababa, Ethiopia), JER, and KBL (Kabul, Afghanistan), whereas the minimum CC_{150s} value of 0.67 is found for the 1968 recording at AFI (Afiamalu, Samoa Islands) compared to the 2018 earthquake record at NIUE (Niue Island), located 607 km away (Fig. S2). Island stations tend to have highly variable site effects due to topography and noise conditions. In addition, many of the island stations have P-wave paths near the downgoing node in the P-wave radiation, thus the signals tend to be higher frequency and more prone to short-period scattering, which can vary between events due to detailed rupture effects. For some of the comparisons (e.g. COP [Copenhagen, Denmark], LAH [Lahore, Pakistan], MSH, PRE [Pretoria, South Africa], SHI), there appears to be some time variation in minute separation for late phases, which is likely primarily related to the separation between WWSSN and broadband stations. However, at least one station (IST [Istabul, Türkiye]) shows a slight variation (~5 s) for the PP arrival compared to station ISK, located only 5 km away, which could be due to site effects or analog record digitization artifacts could also be the cause of the discrepancy. Almost all of the short-length comparisons and some of the full-length comparisons that were made for station pairs separated by large distances (>500 km) show good visual agreement and high cross-correlation coefficients (e.g., LPA [La Plata, Argentina], SDB [Sá Da Bandeira, Angola] in Fig. S2).

The 1965 M_s 7.4 and 2020 M_w 7.4 earthquakes

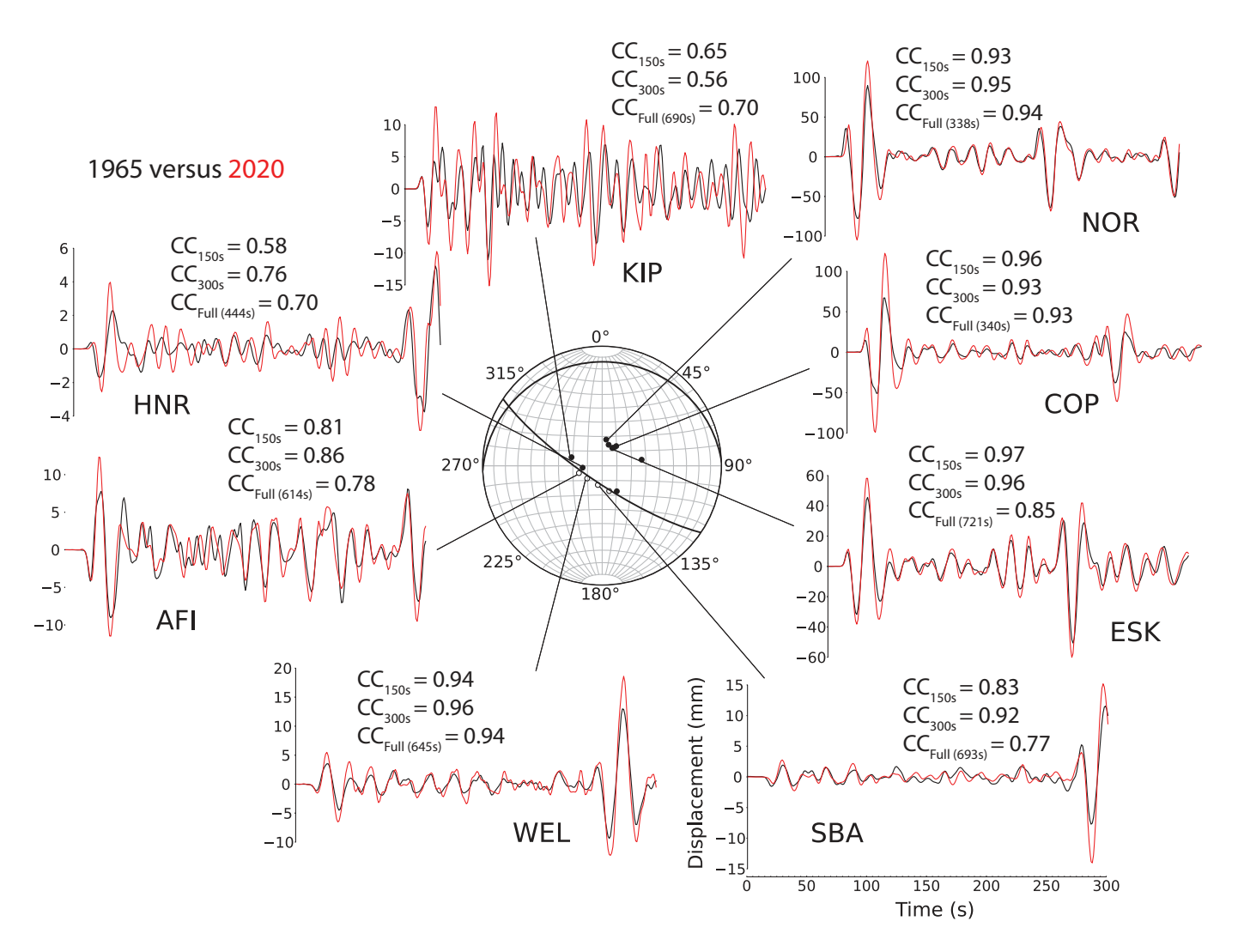
A selection of the total number of seismogram pairs, and first-motion polarities, for the 1965 and 2020 La Crucecita events are shown in Figure 4. Additional waveform comparisons are shown in Figure S3. Table S2 provides information about the recordings. Station ESK has normalized correlation coefficients $CC_{150s} = 0.97$, $CC_{300s} = 0.96$, and $CC_{Full721s} = 0.85$, with the 2020 event having about 25% larger P amplitude. Other stations

show similar amplitude enhancement for the 2020 event. In contrast, Singh *et al.* (2023) find that the 2020 event was about 15% lower amplitude than the 1965 event for the P wave on the Galitzin record at DBN (DeBilt, Netherlands), but slightly larger for the surface waves. Nodal stations SBA (Scott Base, Antarctica), WEL (Wellington, New Zealand), and AFI have CC_{150s} values exceeding 0.81 with stations KIP (Kipapa, Hawaii) and HNR, both with very complex nodal signals, having lower values of 0.65 and 0.58, respectively. CC_{300s} values exceed 0.9 for all the stations in Figure 4 except for HNR, AFI, and KIP, and CC_{Full} values range from 0.70 at KIP and HNR to 0.94 at WEL.

Significance of results

The ideal situation for waveform comparisons between events is to have collocated stations, as is the case in Figures 3 and 4 (except for station LAH); however, because of network changes over the decades, collocated stations are not always possible. Therefore, expanded azimuthal and ray parameter coverage is provided by comparing nearby recordings when collocated stations do not exist. Differences in receiver structure and propagation effects, particularly distance from the source, can then affect the waveforms. For the 1968 and 2018 Pinotepa and 1965 and 2020 La Crucecita recordings, for varying time windows, we plot the instrument-equalized waveform correlation coefficients as a function of epicentral distance difference between the stations used in each comparison in Figure S4. For 150-s-long P-wave waveform segments, there is only a minor effect on waveform correlations for epicentral distance differences up to 700 km, but longer time windows show stronger decorrelation as the difference increases, primarily due to PP-P differential time variations. Similar distributions are found if the correlation coefficients are plotted versus the distance between the stations. Scatter in the measurements exists at all station offsets, which is attributable to the analog record digitization issues discussed earlier. The limited decrease of waveform correlations for 150 s time windows as a function of distance between stations is consistent with the similarity between short-duration waveforms at a given station for events at different positions along the subduction zone. This reinforces the limitations of single-station comparisons for assessing the similarity of the rupture distribution.

We establish the significance of the overall cross-correlation values found for the comparisons between the 1968 and 2018 Pinotepa and the 1965 and 2020 La Crucecita events by considering correlations for WWSSN-equalized waveforms of all four events with three other $M \geq 7.0$ underthrusting earthquakes in the Oaxaca region since 1995. Figure 5 shows the median and quartile distributions, as well as the minimum and maximum ranges, of maximum correlation coefficients for each event pair for varying time windows. For the time windows using 300 s of data and the full extent of the digitized waveforms, we restricted our analysis to WWSSN stations that had a broadband station

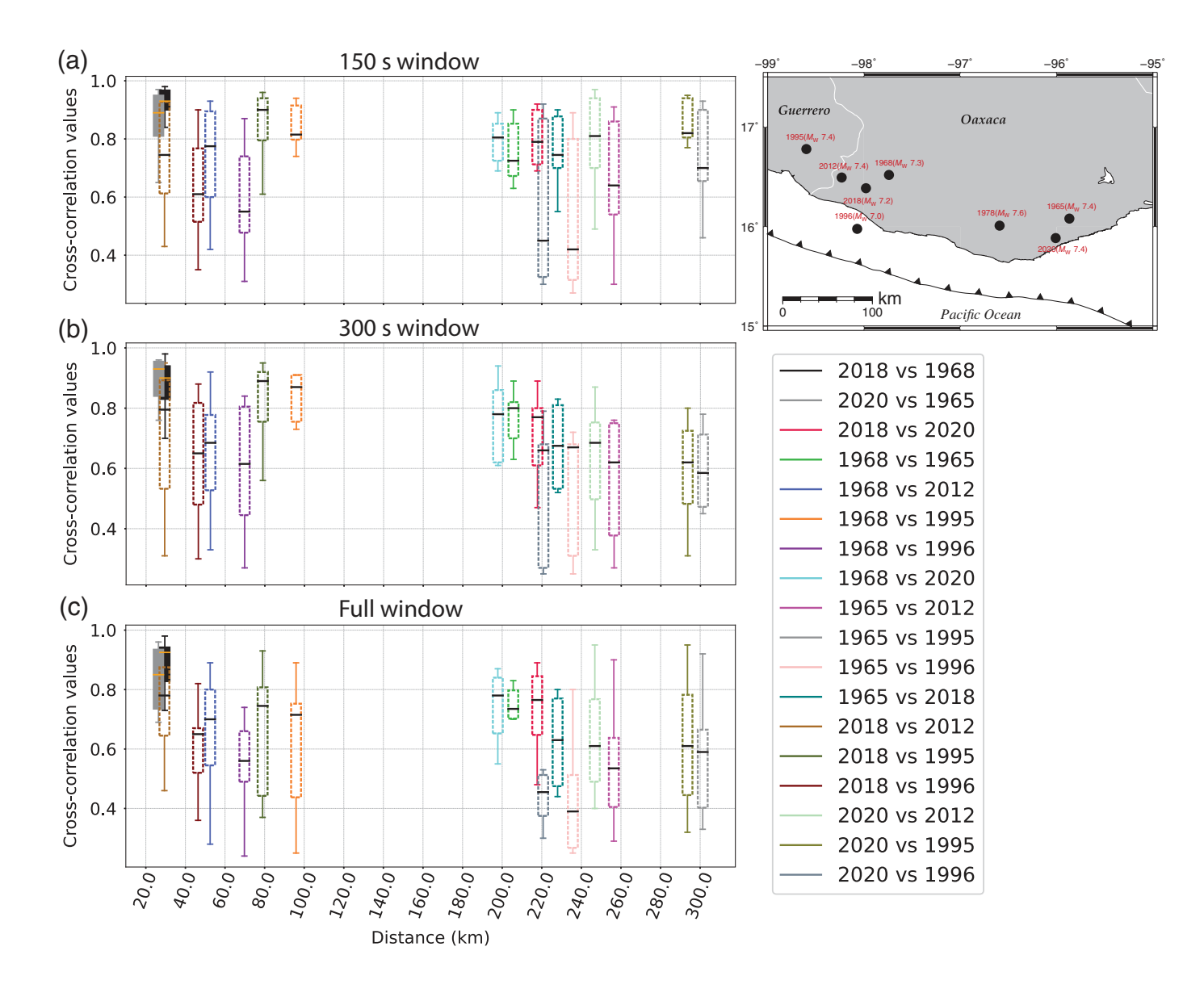


within 150 km. Contemporary broadband digital recordings with good azimuthal distribution are collected for the additional events in 1995, 1996, and 2012 listed in Table S3, and the data are processed in the same way as the 2018 and 2020 events. The waveform data sets are then each cross-correlated with the four main events, again using a mix of collocated and nearby station pairs. The normalized cross-correlation coefficients are plotted versus the distance between the U.S. Geological Survey National Earthquake Information Center (USGS-NEIC) epicenters for each event pair, which have only minor differences relative to using SSN epicenters.

Even though the median correlations of the 1968–2018 and 1965–2020 events pairs rank amongst the highest for the 150 s time windows, little variation is observed as a function of event separation, indicating the intrinsic limitations for inferring source overlap. However, for the 300 s and total time windows, there is a significant decrease in median correlation for source separations greater than 30–40 km. This is very similar to the sensitivity to location found using very long single-station recordings spanning surface waves by Singh *et al.* (2023). The 1968 and 2018 Pinotepa and 1965 and 2020 La Crucecita pairs are thus inferred to have a strong overlap of

Figure 4. Examples of waveform comparisons for the 23 August 1965 $M_{\rm s}$ 7.4 La Crucecita event (black traces) and the 23 June 2020 $M_{\rm w}$ 7.4 La Crucecita event (red traces), showing 300 s of body-wave arrivals for selected stations. The compressional (black circles) and dilational (open circles) *P*-wave first motions of all station pairs and the *P*-wave nodal plane solution for the 1965 event from Chael and Stewart (1982) are shown on an equal-area projection of the lower focal hemisphere. Waveform pairs are shown with WWSSN instrument response displacement amplitudes. Additional waveform comparisons are shown in Figure S3. The high-waveform cross-correlations and the good azimuthal coverage of stations show that the 1965 and the 2020 events are essentially repeated earthquakes with the 2020 events being 15%–20% larger.

their source rupture zones. The 2018 Pinotepa and adjacent 2012 Ometepec events (Fig. 1) have the next highest median correlation, yet well-resolved rupture zones for those events (e.g., Graham et al., 2014; Li et al., 2020; Dominguez et al., 2022) are nearby, but do not overlap. Nevertheless, the 1968 Pinotepa and 2012 Ometepec correlation must be significantly lower, consistent with the spatial offset of their hypocenters exceeding 30 km.



Adding to the maximum cross-correlation values for discrete time windows shown in Tables S1 and S2 and in the whisker plots in Figure 5, we analyze maximum cross-correlation coefficients as a function of window size, which range from 100 s to the maximum length of the digitized trace at each station in 5 s increments. This reduces the arbitrariness of the choice of window length and potential anomalous low cross-correlation coefficients due to errors in the manual digitization. Figures S5 and S6 show the results of maximum cross-correlation values as a function of window size for each station pair for the 1968-2018 Pinotepa and 1965-2020 La Crucecita events pairs, respectively. In addition to comparing the cross-correlation functions of the Pinotepa and La Crucecita event pairs with the correlations between the traces of 1965, 1968, 2018, and 2020 events with the data from 1995, 1996, and 2012, and because not all stations had available data for the latter events, we also test the significance of the observed cross-correlation functions by cross-correlating the 1968 and 1965 events with randomized phase spectrum versions of the 2018 and 2020 events,

Figure 5. Whisker (box) plots of all station correlations for each event pair for the WWSSN equalized waveforms filtered in the passband 5-100 s and plotted versus distance between the U.S. Geological Survey National Earthquake Information Center (USGS-NEIC) hypocenters. (a) 150, (b) 300 s windows, and (c) the full length available for each of the digitized WWSSN records (see Tables S1, S2). Black horizontal bars indicate medians, 25 quartile ranges are shown by the dashed colored boxes, and the maximum and minimum values ranges are shown with vertical lines. The comparison between the 2018 and 1968 events and the 2020 and 1965 events are shown with black and gray filled boxes, respectively, and their median values are shown with an orange horizontal bar. Note that the median correlations degrade significantly for event separations exceeding 30 km for the longer time windows, with the 1965-2020, and 1968-2018 event pairs having the highest correlation distributions for the 300 s and long (full) time windows. Top right inset shows the epicentral location of all the earthquakes used in the analysis.

respectively. One hundred bootstrap realizations for the random phase data are computed by utilizing the same amplitude spectrum as the original 2018 and 2020 traces but randomizing the phase spectra. For the 1968 and 2018 Pinotepa earthquakes, the cross-correlation of the data remains well above the mean and standard deviation of the bootstrap realizations for almost all stations except for stations LAH, RAB (Rabaul, New Britain), and SHI, where the correlation coefficient degrades for a few window sizes (Fig. S5). Stations RAB and LAH particularly exemplify the importance of analyzing the full range of maximum cross-correlations for different time windows because both present a local degradation of the correlation coefficient for windows around 300 s. For the 1965 and 2020 La Crucecita events, the data remain well above the bootstrapped realizations for all stations. The striking robustness of the higher correlations for the 1968-2018 Pinotepa and 1965-2020 La Crucecita earthquakes strengthens the hypothesis that the two earthquake pairs are true repeating events.

Discussion

The rupture complexity of large, shallow earthquakes in subduction zones can be characterized to first order using the asperity model (Lay and Kanamori, 1981), which attributes seismogram complexity to patchy distributions of large slip on the fault during rupture. Whether the slip heterogeneity is stable over multiple ruptures is linked to the fundamental frictional nature of the asperities, which is not generally resolved (e.g., Thatcher, 1989; Scholz, 1998; Schwartz, 1999; Park and Mori, 2007). Structural controls such as plate boundary topography on slip may persist for multiple cycles, whereas hydrological controls such as pore pressure may be much more variable, and the nonlinearity of frictional events can intrinsically cause variations in seismic radiation from similar source regions. Very large $(M_w \ge 7.8)$ earthquakes tend to have complex slip distributions and many decades between events, so there are only a few cases where nearby comparable size ruptures have been evaluated for seismic radiation similarity: 1952-2003 Tokachi-Oki, Japan (Kobayashi et al., 2021), 1942-2016 Ecuador (Ye et al., 2016), and 1943-2015 Illapel, Chile (Tilmann et al., 2016). In all three cases, the events were deemed to be "quasi-repeaters," with some common largeslip zones but an additional slip patch for one member of each pair that weakens the signal correlations.

Observations of small repeating earthquakes located in regions of predominantly slow-slip deformation indicate that isolated persistent asperities are more likely to produce very similar seismic radiation (e.g., Vidale *et al.*, 1994; Nadeau and Johnson, 1998; Uchida *et al.*, 2004; Dominguez *et al.*, 2016; Shaddox and Schwartz, 2019). Given that major ($M_{\rm w}$ 7.2–7.8) earthquakes in the Mexican subduction zone have been characterized as short recurrence time (30–50 yr) ruptures with spatially concentrated slip distributions that give rise to similar simple teleseismic long-period waveforms (e.g., Chael and Stewart, 1982; Singh and Mortera, 1991; Hjörleifsdóttir *et al.*,

2016), the prospect of detecting persistent asperity failure is higher along Mexico than in other subduction zones where ruptures tend to be more complex and less frequent. Not surprisingly, seismograms recorded by WWSSN short-period stations reveal clear differences between the 1965, 1968, and 1978 Oaxaca events that have similar long periods (Tajima, 1984), presumably due to dynamic rupture effects and details of the slip distribution, so the similarity of seismic radiation for large events is likely to diminish for short-period signals.

The teleseismic body-wave waveform comparison between the 1968 $M_{\rm s}$ 7.1 and the 2018 $M_{\rm w}$ 7.2 Pinotepa events presented in this work is one of the most comprehensive data sets for comparing historical earthquakes that occurred in close proximity because it includes numerous long (>300 s duration) records at stations with a good azimuthal distribution from the source. The comparison shows high similarity between the two earthquakes for periods >5 s. The seismogram amplitudes for the 1968 earthquake are systematically slightly larger than for the 2018 earthquake, suggesting that the former had a larger magnitude. This observation is hard to assess given that not all the stations are collocated and differences in amplitude could be due to local effects as well as instrument gain errors. The 1965 M_s 7.4 and 2020 $M_{\rm w}$ 7.4 La Crucecita events have fewer waveform comparisons, but similarly high maximum cross-correlation coefficients, with the 2020 P waveforms being on average about 25% larger.

The pronounced similarity between signals at different azimuths indicates that each event pair ruptured source areas with similar depth and faulting geometry within ~30 km spatial uncertainty. Chael and Stewart (1982) modeled the 1965 and 1968 events with simple trapezoidal source time functions with durations of ~16 s that suggest source dimensions of ~30 km. They suggest that these earthquakes broke different smooth asperities with similar fault areas and variable amounts of slip. Singh and Mortera (1991) determine similar trapezoidal source time functions for the 1965 and 1968 events from WWSSN stations and Galitzin-Wilip instruments at stations DeBilt, Netherlands (DBN), and Stuttgart, Germany (STU). The latter instruments also provided similar quasi-triangular source time functions for the 22 March 1928 and 4 August 1928 events near these events. The moment-rate functions estimated by the SCARDEC method (see Data and Resources; Vallée and Douet, 2016) for the 2018 and 2020 events are also relatively simple triangular functions with a total duration of 10-5 s, with the peak moment rate being about three times larger for the 2020 event. Extensive broadband seismic and geodetic observations have been used to invert for finite-fault sources for the 2018 Pinotepa earthquake (e.g., Tung et al., 2019; Li et al., 2020) and 2020 La Crucecita (e.g., Melgar et al., 2020; Guo et al., 2021, Wen et al., 2021; Yan et al., 2022).

Figure 6 shows the large-slip (>1 m) regions determined for the 2018 (Li *et al.*, 2020) and 2020 (Yan *et al.*, 2022) events. Slip models for the 2018 event show either one or two main slip

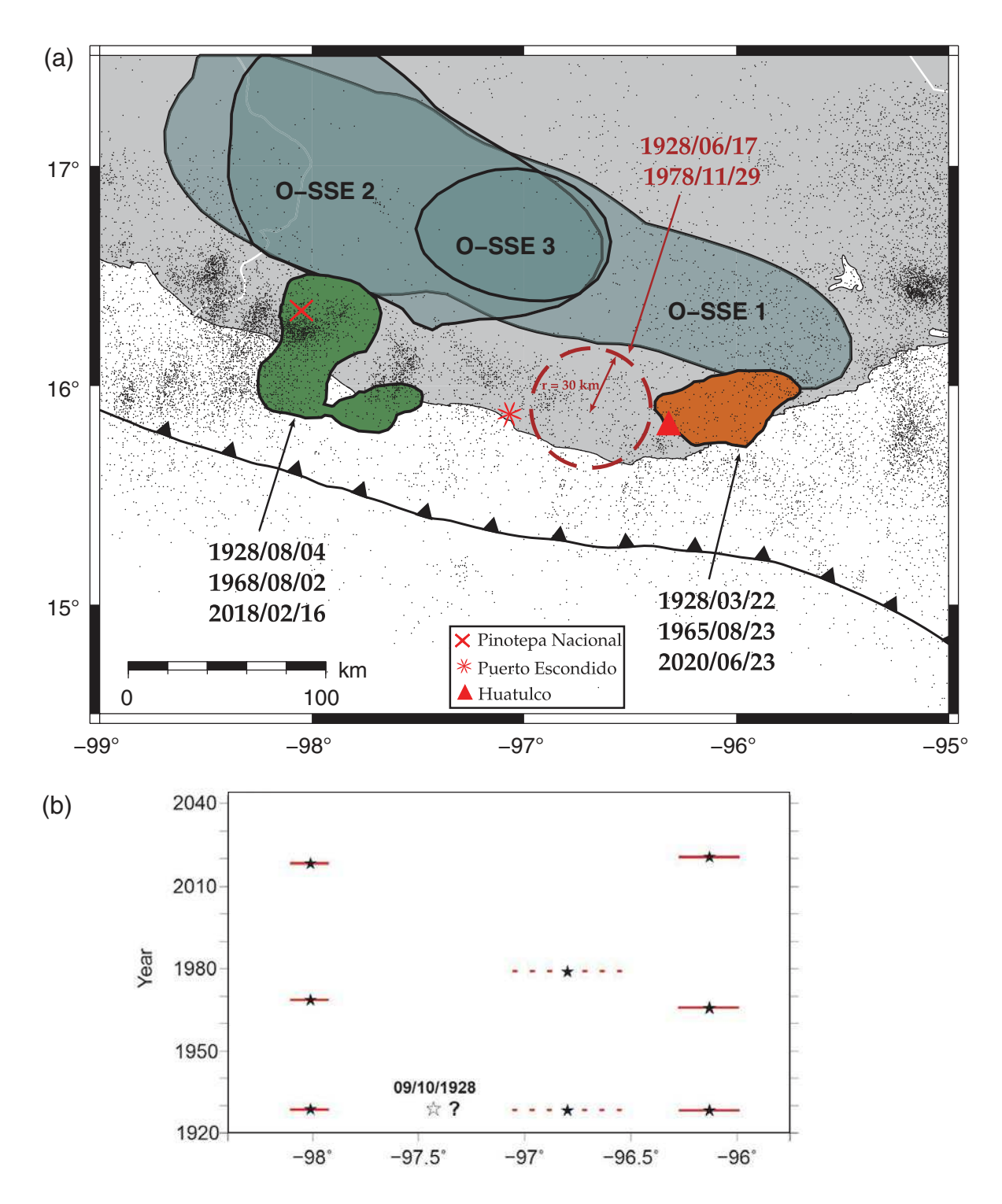


Figure 6. Summary of earthquakes and slow-slip events in the Oaxaca subduction zone. (a) Large-slip regions for the 2018 Pinotepa earthquake (Li *et al.*, 2020) and the 2020 La Crucecita earthquake (Yan *et al.*, 2022) are highlighted in green and orange patches, respectively. The corresponding persistent asperity regions are inferred to have ruptured in the indicated prior events based on the waveform similarity analysis. An estimate of the slip area for the 1978 Oaxaca event (dashed circle) based on the source duration found by Chael and Stewart (1982) is the inferred location of a persistent asperity that also ruptured in 1928. Slip regions of Oaxaca slow-slip events O-SSE1 (June 2017 to February 2018), O-SSE2 (February 2019 to July 2019), and O-SSE3 (April

2020 to 23 June 2020) are indicated by gray patches (Cruz-Atienza et al., 2021). Black data points represent the regional earthquake catalog from Servicio Sismológico Nacional (SSN) spanning from 2000 to 2017 ($M \ge 3.6$). Red symbols represent the location of the most populated cities in the region. (b) Timeline of repeated earthquakes along the Oaxaca subduction zone, reproduced from Singh et al. (2023; fig. 17b). The red lines indicate the inferred rupture area diameters for the events assuming that repeated events share the same source dimensions. The "?" symbol associated with the event on 9 October 1928 denotes large uncertainty in its location along the subduction zone.

zones, with the dimensions of the main patch being about 70 km \times 50 km. The source area for the 2020 event is about 35 km \times 70 km, and is generally consistent among various inversions, as shown in Yan *et al.* (2022). These sources are within the \sim 30 km spatial uncertainty inferred for the azimuthally varying correlation coefficient medians; therefore, it is reasonable to infer that the 1965 and 1968 ruptures significantly overlapped the corresponding slip zones for the recent events. The same asperities likely broke in the 1928 events in both source regions based on the waveforms analyzed by Singh *et al.* (2023). It appears that the asperities in these two regions have persisted for at least three events, and plausibly were ruptured in the preseismic records events in each region noted in the Introduction.

The 1978 Oaxaca earthquake source dimension is estimated to have a radius of about 30 km based on the 15 s duration trapezoidal source model determined by Stewart *et al.* (1981), and this is indicated in Figure 6. The similar waveforms for the nearby 1928 event analyzed by Singh *et al.* (2023) suggest that a corresponding persistent asperity within this source region failed in both events.

Slow-slip events are now well documented along the downdip plate boundary fault throughout the Oaxaca (Fig. 6) and Guerrero margins. Cruz-Atienza et al. (2021) showed that a slow-slip event (O-SSE1), which may have been perturbed and accelerated by dynamic stresses from the great 2017 $M_{\rm w}$ 8.2 Tehuantepec earthquake, increased the Coulomb failure stress (CFS) around the 2018 Pinotepa earthquake, and the afterslip of that event extended into the down-dip slow-slip region where a more localized slow-slip event (O-SSE2) occurred in 2019, while dynamic stresses may have reactivated slow slip along the Guerrero margin. Slow-slip event O-SSE1 extended to near the 2020 La Crucecita source region and produced a CFS increase in that source region as well as in the 1978 rupture zone region. A subsequent slow-slip event (O-SSE3) was initiated along the central Oaxaca seismic gap two months prior to the 2020 La Crucecita event.

The central Oaxaca coastal region can be viewed as a mature seismic gap, with the northwestern portion of the gap not having ruptured since 1928, whereas the southeastern portion ruptured a persistent asperity in 1928 and 1978. Figure 6b shows a timeline of repeated earthquakes along the longitudinal range of the Oaxaca subduction zone from Singh et al. (2023; fig. 17b in their article). The central coastal region exhibits a high potential for subduction zone earthquakes, given the elapsed time since the last ruptures. Geodetic inferred coupling along the seismic gap region is quite high (Rousset et al., 2016), so plausible scenarios for future major events include rerupture of the persistent asperity that failed in 1978 in an $M_{\rm w} \sim 7.6$ event; rupture of that asperity plus the adjacent region to the northwest that last failed in 1928 in a larger $M_{\rm w} \sim 7.8$ event, or separate rupture of both regions. For the Mexican subduction zone, which evidently can be characterized as having well-defined asperities that can host repeating events, the effect of CFS change increases in the seismogenic zone as a consequence of accelerating slow-slip events down-dip has been shown observationally (Radiguet et al., 2016; Cruz-Atienza et al., 2021) and by numerical modeling (Li and Gabriel, 2024). There have likely been many slow-slip events down-dip since the last ruptures, but it is possible that any of the three scenarios may be preceded by slow-slip events such as O-SSE1, O-SSE2, or O-SSE3. Although the population density in the region is low, damage comparable to that for the 2018 and 2020 earthquakes is likely. Given the occurrence of the latter two events and their localized strain reductions, it would appear that re-rupture of the entire coastal region in a 1787 size event is not likely in the short term.

Conclusions

Major plate boundary thrust events along Oaxaca tend to involve rupture of isolated asperities with source durations of about 15 s that result in relatively simple teleseismic P waveforms for periods >5 s. Evidence for overlap of the asperities that rupture with intervals of about 45–50 yr is provided by the similarity of the long-period body-wave trains at azimuthally varying stations for the 1968 and 2018 Pinotepa earthquakes and 1965 and 2020 La Crucecita earthquakes, bolstering waveform similarity from long-duration seismograms at individual stations in Europe that include prior events in both regions in 1928. The strength of waveform correlations suggests that the separation distance between sequential events in a given region is less than 30 km, which is less than the ~50 to 70 km dimensions from well-resolved finite-fault models for the most recent events. We infer that these events involve the rupture of persistent asperities over three earthquake cycles, and an additional pair of events in 1928 and 1978 also appears to involve a persistent asperity in the central Oaxaca region. This is the best-documented case of persistent asperity areas for major earthquakes that involve very simple ruptures. Slow-slip events have been documented along the down-dip plate interface prior to both the 2018 and 2020 ruptures, and plausibly will precede future rupture of the 1978 zone and/or an adjacent portion of the central Oaxaca region that has not failed since 1928.

Data and Resources

The historical World-Wide Standardized Seismograph Network (WWSSN) seismograms were obtained from the "Historical Seismogram Search System" archived at the Earthquake Research Institute (ERI) of the University of Tokyo (http://wwweic.eri.u-tokyo.ac.jp/susu/index_en.html). The list of available WWSSN seismograms is available at http://wwweic.eri.u-tokyo.ac.jp/wwssn/filmlist.html. All other seismic data used are openly available from the Incorporated Research Institutions for Seismology Data Management Center (IRIS-DMC; http://ds.iris.edu/wilber3/find_event). The SCARDEC method is available at http://scardec.projects.sismo.ipgp.fr/. All websites were last accessed in October 2024. The supplemental material for this article includes three tables and six additional figures. The tables show a summary of the data and results, as well as the location of all the events

analyzed and the six additional figures are relevant to the location of the stations, the comparison of the traces for each station pair analyzed, and the significance of the results.

Declaration of Competing Interests

The authors acknowledge that there are no conflicts of interest recorded.

Acknowledgments

This work would not have been possible without the valuable help of Satoko Murotani and Kenji Satake, who provided scanned copies of the World-Wide Standardized Seismograph Network (WWSSN) paper records of the 1965 La Crucecita earthquake from the archives of the Earthquake Research Institute (ERI) of The University of Tokyo. Krisha Singh kindly shared his article on repeating earthquakes along Mexico and Chengli Liu discussed his work on Mexican earthquakes with them. Carlos Villafuerte shared data for the mapping of the Oaxaca slow-slip events. The authors appreciate discussions with Hiroo Kanamori on historic seismograms for Mexican earthquakes. An anonymous reviewer and Luis Antonio Domingues provided helpful reviews of the article. L. Ye's subduction zone earthquake research is supported in part by the National Key R&D Program of China (2023YFF0803200). T. Lay's research on earthquake processes is supported by the National Science Foundation (NSF) Grant EAR-1802364.

References

- Astiz, L., and H. Kanamori (1984). An earthquake doublet in Ometepec, Guerrero, Mexico, *Phys. Earth Planet. In.* **34**, 24–45.
- Astiz, L., H. Kanamori, and H. Eissler (1987). Source characteristics of earthquakes in the Michoacan seismic gap in Mexico, *Bull. Seismol. Soc. Am.* 77, 1326–1346.
- Benioff, H. (1955). Earthquake seismographs and associated instruments *Adv. Geophys.*, **2**, 219–275, doi: 10.1016/S0065-2687(08) 60314-3.
- Chael, E. P., and G. S. Stewart. (1982). Recent large earthquakes along the Middle American trench and their implications for the subduction process, *J. Geophys. Res.* **87**, 329–338.
- Cruz-Atienza, V. M., J. Tago, C. Villafuerte, M. Wei, R. Garza-Girón, L. A. Dominguez, V. Kostoglodov, T. Nishimura, S. I. Franco, J. Real, et al. (2021). Short-term interaction between silent and devastating earthquakes in Mexico, Nat. Commun. 12, 1–14.
- Dominguez, L. A., T. Taira, V. M. Cruz-Atienza, A. Iglesias, C. Villauerte, D. Legrand, X. Pérez-Campos, and M. Raggi (2022). Interplate slip rate variations between closely spaced earthquakes in southern Mexico: The 2012 Ometepec and 2018 Pinotepa Nacional thrust events, *J. Geophys. Res.* 127, e2022JB024292, doi: 10.1029/2022JB024292.
- Dominguez, L. A., T. Taira, and M. A. Santoyo (2016). Spatiotemporal variations of characteristic repeating earthquake sequences along the Middle America Trench in Mexico, *J. Geophys. Res.* **121**, 8855–8870.
- Dost, B., and H. W. Haak (2006). Comparing waveforms by digitization and simulation of waveforms for four Parkfield earthquakes observed in station DBN, the Netherlands, *Bull. Seismol. Soc. Am.* **96,** no. 4B, S50–S55.

- Graham, S. E., C. DeMets, E. Cabral-Cano, V. Kostoglodov, A. Walpersdorf, N. Cotte, M. Brudzinski, R. McCafrey, and L. Salazar-Tlaczani (2014). GPS constraints on the $M_{\rm W}=7.5$ Ometepec earthquake sequence, southern Mexico: Coseismic and post-seismic deformation, *Geophys. J. Int.* **199**, 200–218.
- Guo, R., H. Yang, Y. Zhu, Y. Zheng, J. Xu, L. Zhang, and C. An (2021). Narrow rupture of the 2020 $M_{\rm W}$ 7.4 La Crucecita, Mexico, Earthquake, *Seismol. Res. Lett.* **92**, 1891–1899.
- Hjörleifsdóttir, V., K. S. Singh, L. Martínez-Peláez, R. Garza-Girón, B. Lund, and C. Ji (2016). Observations of large earthquakes in the Mexican subduction zone over 110 years, EGU General Assembly Conference Abstracts, EPSC2016-10827 pp.
- Kanamori, H., and K. C. McNally (1982). Variable rupture mode of the subduction zone along the Ecuador-Colombia coast, *Bull. Seismol. Soc. Am.* **72**, 1241–1253.
- Kobayashi, H., K. Koketsu, H. Miyake, and H. Kanamori (2021). Similarities and differences in the rupture processes of the 1952 and 2003 Tokachi-Oki earthquakes, *J. Geophys. Res.* **126**, no. 1, e2020JB020585, doi: 10.1029/2020JB020585.
- Lay, T. (2018). A review of the rupture characteristics of the 2011 Tohoku-Oki earthquake, *Tectonophysics* **733**, 4–36.
- Lay, T., and H. Kanamori (1981). An asperity model of large earthquake sequences, in *Earthquake Prediction: An International Review*, D. W. Simpson and P. G. Richards (Editors) Vol. 4, 579–592, doi: 10.1002/SERIES5068.
- Lay, T., H. Kanamori, C. J. Ammon, M. Nettles, S. N. Ward, R. C. Aster, S. L. Beck, S. L. Bilek, M. R. Brudzinski, R. Butler, *et al.* (2005). The great Sumatra-Andaman earthquake of 26 December 2004, *Science* 308, 1127–1133.
- Li, D., and A. A. Gabriel (2024). Linking 3D long-term slow-slip cycle models with rupture dynamics: The nucleation of the 2014 $M_{\rm W}$ 7.3 Guerrero, Mexico earthquake, $AGU\,Adv.$ 5, no. 2, e2023AV000979, doi: 10.1029/2023AV000979.
- Li, Y., X. Shan, C. Zhu, X. Qiao, L. Zhao, and C. Qu (2020). Geodetic model of the 2018 $M_{\rm W}$ 7.2 Pinotepa, Mexico, earthquake Inferred from InSAR and GPS data, *Bull. Seismol. Soc. Am.* 110, 1115–1124.
- Liu, C., T. Lay, Y. Bai, P. He, and X. Xiong (2023). Coseismic slip model of the 19 September 2022 $M_{\rm W}$ 7.6 Michoacan, Mexico, earthquake: A quasi-repeat of the 1973 $M_{\rm W}$ 7.6 rupture, Seism. Record 3, 57–68.
- Melgar, D., A. Ruiz-Angulo, X. Pérez-Campos, B. W. Crowell, X. Xu, E. Cabral-Cano, M. R. Brudzinski, and L. Rodriguez-Abreu (2020). Energetic rupture and tsunamigenesis during the 2020 $M_{\rm W}$ 7.4 La Crucecita, Mexico earthquake, *Seismol. Res. Lett.* **92**, 140–150.
- Nadeau, R. M., and L. R. Johnson (1998). Seismological studies at Parkield VI: Moment release rates and estimates of source parameters for small repeating earthquakes, *Bull. Seismol. Soc.* Am. 88, 790–814.
- Nishenko, S. P., and S. K. Singh (1987). The Acapulco-Ometepec, Mexico, earthquakes of 1907-1982: Evidence for a variable recurrence history, *Bull. Seismol. Soc. Am.* 77, 1359–1367.
- Oliver, J., and L. M. Murphy (1971). WWNSS—Seismology's global network of observing stations, *Science* **174**, 254–261.
- Park, S. C., and J. Mori (2007). Are asperity patterns persistent? Implication from large earthquakes in Papua New Guinea, J. Geophys. Res. 112, no. B3, doi: 10.1029/2006JB004481.

- Peterson, J., and C. R. Hutt (2014). World-wide standardized seismograph network: A data users guide, *U.S. Geol. Surv. Open-File Rept.* 2014-1218, US Department of the Interior, 82 pp.
- Press, F., M. Ewing, and F. Lehner (1958). A long-period seismograph system, *Eos Trans. AGU* **39**, 106–108.
- Radiguet, M., H. Perfettini, N. Cotte, A. Gualandi, B. Valette, V. Kostoglodov, T. Lhomme, A. Walpersdorf, E. Cabral Cano, and M. Campillo (2016). Triggering of the 2014 $M_{\rm W}$ 7.3 Papanoa earth-quake by a slow slip event in Guerrero, Mexico, *Nature Geosci.* 9, no. 11, 829–833.
- Rousset, B., C. Lasserre, N. Cubas, S. Graham, M. Radiguet, C. DeMets, A. Socquet, M. Campillo, V. Kostoglodov, E. Cabral-Cano, et al. (2016). Lateral variations of interplate coupling along the Mexican subduction interface: Relationships with long-term morphology and fault zone mechanical properties, Pure Appl. Geophys. 173, 3467–3486.
- Santoyo, M. A., S. K. Singh, T. Mikumo, and M. Ordaz (2005). Spacetime clustering of large thrust earthquakes along the Mexican subduction zone: An evidence of source stress interaction, *Bull. Seismol. Soc. Am.* 95, 1856–1864.
- Satake, K., H. Tsuruoka, S. Murotani, and K. Tsumura (2020). Analog seismogram archives at the Earthquake Research Institute, the University of Tokyo, Seismol. Res. Lett. 91, 1384–1393.
- Schneider, C. A., W. S. Rasband, and K. W. Eliceiri (2012). NIH Image to ImageJ: 25 years of image analysis, Nat. Methods 9, 671–675.
- Scholz, C. H. (1998). Earthquakes and friction laws, *Nature* 391, 37–42.
 Schwartz, S. Y. (1999). Noncharacteristic behavior and complex recurrence of large subduction zone earthquakes, *J. Geophys. Res.* 104, 23,111–23,125.
- Shaddox, H. R., and S. Y. Schwartz (2019). Subducted seamount diverts shallow slow slip to the forearc of the northern Hikurangi subduction zone, New Zealand, *Geology* 47, no. 5, 415–418.
- Singh, S. K., and F. Mortera (1991). Source time functions of large Mexican subduction earthquakes, morphology of the Benioff zone, age of the plate, and their tectonic implications, *J. Geophys. Res.* **96**, 21,487–21,502.
- Singh, S. K., L. Astiz, and J. Havskov (1981). Seismic gaps and recurrence periods of large earthquakes along the Mexican subduction zone: A reexamination, *Bull. Seismol. Soc. Am.* 71, 827–843.
- Singh, S. K., R. D. Corona-Fernandez, M. A. Santoyo, and A. Iglesias (2023). Repeating large earthquakes along the Mexican Subduction Zones, Seismol. Res. Lett. 95, 458–478.
- Singh, S. K., M. Rodriguez, and J. M. Espinadola (1984). A catalog of shallow earthquakes of Mexico from 1900 to 1981, *Bull. Seismol. Soc. Am.* **74**, 267–279.
- Stewart, G. S., E. P. Chael, and K. C. McNally (1981). The November 29, 1978, Oaxaca, Mexico, earthquake: A large simple event, *J. Geophys. Res.* **86,** 5053–5060.
- Suárez, G., and P. Albini (2009). Evidence for great tsunamigenic earthquakes (*M* 8.6) along the Mexican subduction zone, *Bull. Seismol. Soc. Am.* **99**, 892–896.

- Suárez, G., D. Ruiz-Barón, C. Chico-Hernández, and F. R. Zúñiga (2020). Catalog of preinstrumental earthquakes in central Mexico: Epicentral and magnitude estimations based on macroseismic data, *Bull. Seismol. Soc. Am.* 110, 3021–3036
- Tajima, F. (1984). Study of the source processes of the 1965, 1968 and 1978 Oaxaca earthquakes using short-period records, *J. Geophys. Res.* **89**, 1867–1873.
- Thatcher, W. (1989). Earthquake recurrence and risk assessment in circum-Pacific seismic gaps, *Nature* **341**, 432–434.
- Tilmann, F., Y. Zhang, M. Moreno, J. Saul, F. Eckelmann, M. Palo, Z. Deng, A. Babeyko, K. Chen, J. C. Báez, *et al.* (2016). The 2015 Illapel earthquake, central Chile: A type case for a characteristic earthquake? *Geophys. Res. Lett.* **43**, 574–583.
- Tung, S., E. J. Fielding, D. P. S. Bekaert, and T. Masterlark (2019).
 Rapid geodetic analysis o subduction zone earthquakes leveraging a 3-D elastic Green's function library, *Geophys. Res. Lett.* 46, 2475–2483
- U. N. A. de México Seismology (2013). Ometepec-Pinotepa Nacional, Mexico earthquake of 20 March 2012 (M_w 7.5): A Preliminary Report, Geofís. Int. 52, 173–196.
- Uchida, N., A. Hasegawa, T. Matsuzawa, and T. Igarashi (2004).

 Pre- and post-seismic slow slip on the plate boundary off
 Sanriku, NE Japan associated with three interplate earthquakes
 as estimated from small repeating earthquake data,

 Tectonophysics 385, 1–15.
- Vallée, M., and V. Douet (2016). A new database of source time functions (STFs) extracted from the SCARDEC method, *Phys. Earth Planet In.* **257**, 149–157.
- Vidale, J. E. W., L. Ellsworth, A. Cole, and C. Morone (1994).
 Variations in rupture process with recurrence interval in a repeated small earthquake, *Nature* 368, 624–626.
- Wen, Y., Z. Xiao, P. He, J. Zang, Y. Liu, and C. Xu (2021). Source characteristics of the 2020 $M_{\rm W}$ 7.4 Oaxaca, Mexico, earthquake estimated from GPS, InSAR, and teleseismic waveforms, *Seismol. Res. Lett.* **92**, 1900–1912.
- Yan, Z., X. Xiong, C. Liu, and J. Xu (2022). Integrated analysis of the $2020\,M_{\rm W}$ 7.4 La Crucecita, Oaxaca, Mexico, earthquake from joint inversion of geodetic and seismic observations, *Bull. Seismol. Soc. Am.* **112**, 1271–1283.
- Ye, L., H. Kanamori, J. P. Avouac, L. Li, K. F. Cheung, and T. Lay (2016). The 16 April 2016, $M_{\rm W}$ 7.8 ($M_{\rm S}$ 7.5) Ecuador earthquake: A quasi-repeat of the 1942 $M_{\rm S}$ 7.5 earthquake and partial re-rupture of the 1906 $M_{\rm S}$ 8.6 Colombia–Ecuador earthquake, *Earth Planet. Sci. Lett.* **454**, 248–258.
- Ye, L., H. Kanamori, and T. Lay (2018). Global variations of large megathrust earthquake rupture characteristics, *Sci. Adv.* **4**, no. 3, eaao4915, doi: 10.1126/sciadv.aao4915.

Manuscript received 26 June 2024 Published online 28 October 2024

Supplementary Materials for

The Repeating Major Earthquakes in the Mexican Subduction Zone Along Oaxaca: Implications for Future Events

Ricardo Garza-Giron^{1,2}, Thorne Lay², Lingling Ye³

1. Department of Geosciences, Warner College of Natural Resources, Colorado State University, Fort Collins, CO, USA, https://orcid.org/0000-0001-9775-9635 (RGG); 2. Department of Earth and Planetary Sciences, University of California, Santa Cruz, Santa Cruz, CA 95064, USA, https://orcid.org/0000-0003-2360-4213 (TL); 3. Department of Earth and Space Sciences, Southern University of Science and Technology, Shenzhen, China (LY).

Correspondence to: r.garza giron@colostate.edu

This PDF file includes:

Tables S1 to S3 Figures S1 to S6

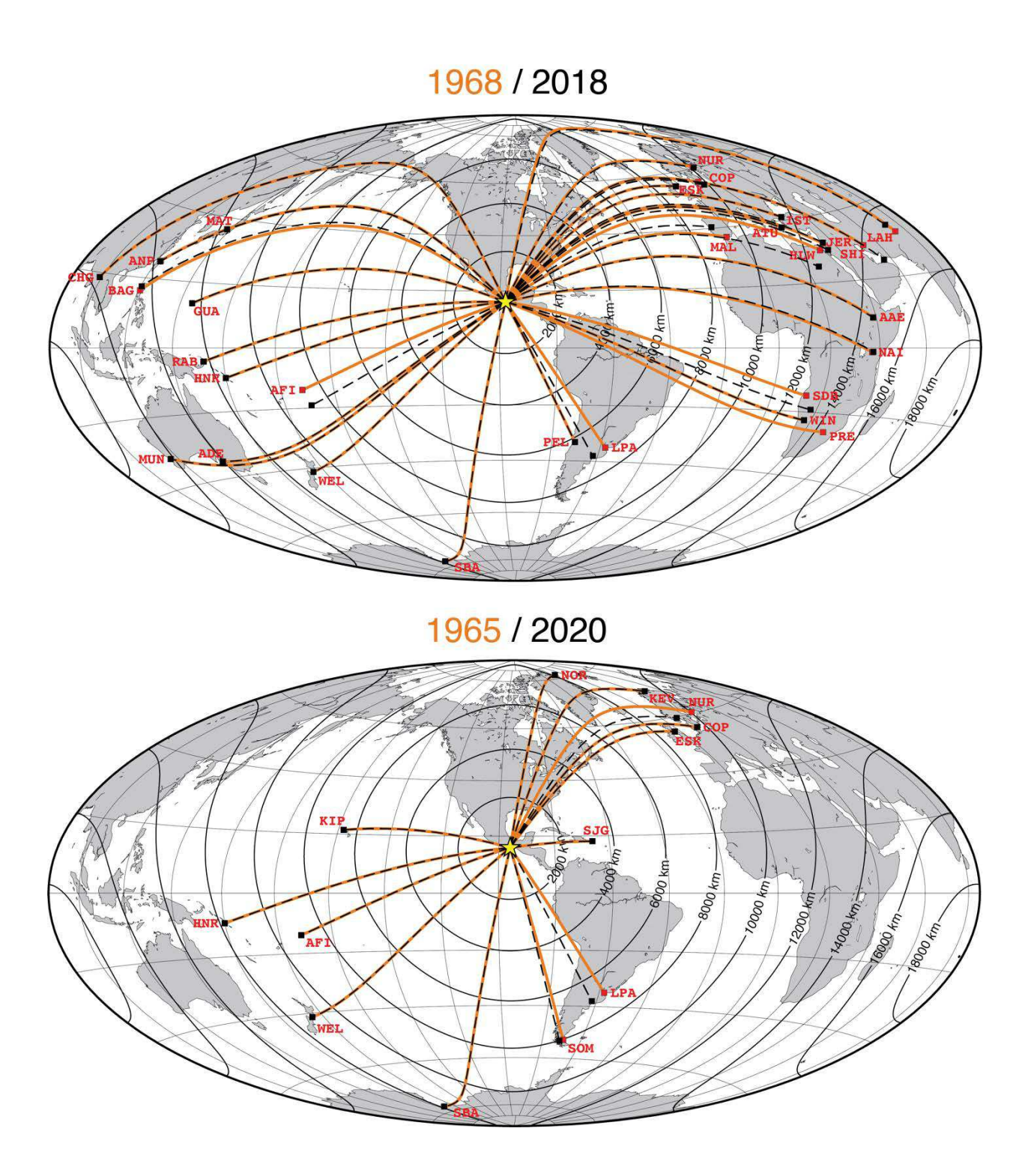


Figure S1. Map showing the distribution of stations used in this study. The great-circle path from the epicenters of the 1965 and 1968 earthquakes to the WWSSN stations are shown in orange and the great-circle paths to the current broad-band stations are shown in black. Red labels show the name of the WWSSN stations (refer to Tables S1 and S2 for information on the broad-band station used for each station pair).

WWSSN code	WWSSN location	Lat wwssn [°]	Lon wwssn [°]	Δ wwssn [°]	BB code	BB location	Lat BB [°]	Lon BB [°]	Δ _{вв} [°]	Station distance [km]	WWSSN MAG	Length of trace [s]	150 s CC	300 s CC	Full CC
AAE	Addis Ababa, Ethiopia	9.03	38.77	130.23	FURI	Mount Furi, Ethiopia	8.9	38.68	130.22	17	1500	339	0.98	0.96	0.95
ADE	Adelaide, Australia	-34.97	138.71	126.4	AUMAR	Marden Senior College, Australia	-34.89	138.64	126.47	11	750	140	0.92	N/A	0.92
AFI	Afiamalu, Samoa Islands	-13.91	-171.78	78.93	NIUE	Niue Island, Niue	-19.08	-169.93	79.12	607	750	450	0.67	0.65	0.61
ANP	Anpu, Taiwan	25.18	121.52	123.36	TATO	Taipei, Taiwan	24.97	121.50	123.52	23	750	734	0.91	0.72	0.77
ATU	Athens, Greece	37.97	23.72	102.93	ATHU	Athens University, Greece	37.97	23.78	102.98	5	1500	565	0.97	0.94	0.92
BAG	Baguio City, Philippines	16.41	120.58	129.79	SZP	Santa, Ilocos Sur, Philippines	17.55	120.46	129.16	127	3000	334	0.72	0.75	0.65
CHG	Chiang Mai, Thailand	18.79	98.98	141.07	CHTO	Chiang Mai, Thailand	18.81	98.94	141.06	4	3000	162	0.95	N/A	0.94
COP	Copenhagen, Denmark	55.68	12.43	87.45	RGN	Ruegen, Germany	54.55	13.32	88.41	138	750	323	0.96	0.74	0.74
ESK	Eskdalemuir, Scotland	55.32	-3.21	79.25	ESK	Eskdalemuir, Scotland	55.32	-3.21	79.25	0	750	497	0.97	0.95	0.94
GUA	Guam, Mariana Islands	13.54	144.91	111.04	GUMO	Guam, Mariana Islands	13.59	144.87	111.06	7	750	593	0.84	0.83	0.73
HLW	Helwan, Egypt	29.86	31.34	112.75	EIL	Eilat, Israel	29.67	34.95	115.35	349	3000	259	0.96	0.77	0.77
HNR	Honiara, Solomon Islands	-9.43	159.95	104.13	HNR	Honiara, Solomon Islands	-9.43	159.95	104.13	0	1500	688	0.90	0.85	0.79
IST	Istanbul, Turkey	41.05	29.0	104.47	ISK	Üsküdar, Istanbul, Turkey	41.06	29.06	104.5	5	1500	408	0.97	0.86	0.94

JER	Jerusalem	31.77	35.2	114.18	UJAP	Al-Auja, Jerico, Palestine	31.95	35.46	114.23	32	3000	117	0.98	N/A	0.98
KBL	Kabul, Afghanistan	34.54	69.04	127.6	KBL	Kabul, Afghanistan	34.54	69.04	127.6	0	6000	210	0.98	N/A	0.96
KTG	Kap Tobin, Greenland	70.42	-21.98	69.9	DBG	Daneborg, Greenland	74.30	-20.22	70.93	436	750	570	0.91	0.77	0.68
LAH	Lahore, Pakistan	31.55	74.33	131.5	NIL	Nilore, Pakistan	33.65	73.27	129.27	253	750	1429	0.90	0.73	0.34
LPA	La Plata, Argentina	-34.91	-57.93	63.85	TRQA	Tornquist, Argentina	-38.06	-61.98	64.07	503	750	479	0.91	0.78	0.74
MAL	Malaga, Spain	36.73	-4.41	83.06	MTE	Manteigas, Portugal	40.40	-7.54	79.79	490	1500	214	0.75	N/A	0.70
MAT	Matsushiro, Japan	36.54	138.21	105.13	MAJO	Matsushiro, Japan	36.54	138.21	105.13	0	3000	767	0.97	0.97	0.95
MSH	Mashhad, Iran	36.31	59.59	123.2	KBL	Kabul, Afghanistan	34.54	69.04	127.6	878	1500	315	0.93	0.43	0.42
MUN	Mundaring, Australia	-31.98	116.21	145.34	MUN	Mundaring, Australia	-31.98	116.21	145.34	0	750	139	0.84	N/A	0.84
NAI	Nairobi, Kenya	-1.27	36.8	132.99	KMBO	Mount Kilimambogo, Kenya	-1.13	37.25	133.36	52	1500	339	0.97	0.94	0.93
NUR	Nurmijärvi, Finland	60.51	24.65	90.52	MEF	Metsahovi, Finland	60.22	24.4	90.59	35	1500	215	0.97	N/A	0.96
PEL	Peldehue, Chile	-33.14	-70.69	55.97	PEL	Peldehue, Chile	-33.14	-70.69	55.97	0	1500	566	0.93	0.85	0.94
PRE	Pretoria, South Africa	-25.75	28.19	129.24	LBTB	Lobatse, Botswana	-25.02	25.60	126.88	273	1500	306	0.74	0.60	0.60
RAB	Rabaul, New Britain	-4.19	152.32	110.07	RABL	Rabaul, New Britain	-4.18	152.16	110.22	17	750	1131	0.72	0.70	0.50
SBA	Scott Base, Antarctica	-77.85	166.76	107.12	SBA	Scott Base, Antarctica	-77.85	166.76	107.12	0	750	431	0.92	0.94	0.94
SDB	Sá Da Bandeira, Angola	-14.93	13.57	114.4	TSUM	Tsumeb, Namibia	-19.2	17.58	118.93	638	1500	395	0.92	0.51	0.96
SHI	Shiraz, Iran	29.64	52.52	125.89	UOSS	University of Sharjah, UAE	24.95	56.20	131.61	636	1500	324	0.96	0.40	0.39

SHL	Shillong, India	25.57	91.88	136.96	SHL	Shillong, India	25.57	91.86	136.97	2	3000	273	0.79	N/A	0.88
SPA	South Pole, Antarctica	-90	0.0	106.39	QSPA	South Pole, Antarctica	-89.93	144.44	106.42	7	750	408	0.96	0.98	0.97
WEL	Wellington, New Zealand	-41.29	174.77	98.72	SNZO	South Karori, New Zealand	-41.31	174.7	98.77	5	750	324	0.94	0.90	0.89
WIN	Windhoek, Namibia	-22.57	17.1	118.93	WIN	Windhoek, Namibia	-22.57	17.1	118.93	0	1500	643	0.95	0.92	0.86

Table S1. Summary of long-period waveform data and results for the comparison between the 1968 earthquake recorded by the WWSSN network and the 2018 earthquake recorded by broad-band (BB) digital stations and converted to WWSSN response. Notation: Δ=Epicentral distance; **BB**=Broad-band; **CC**=Cross-correlation.

1968 vs 2018

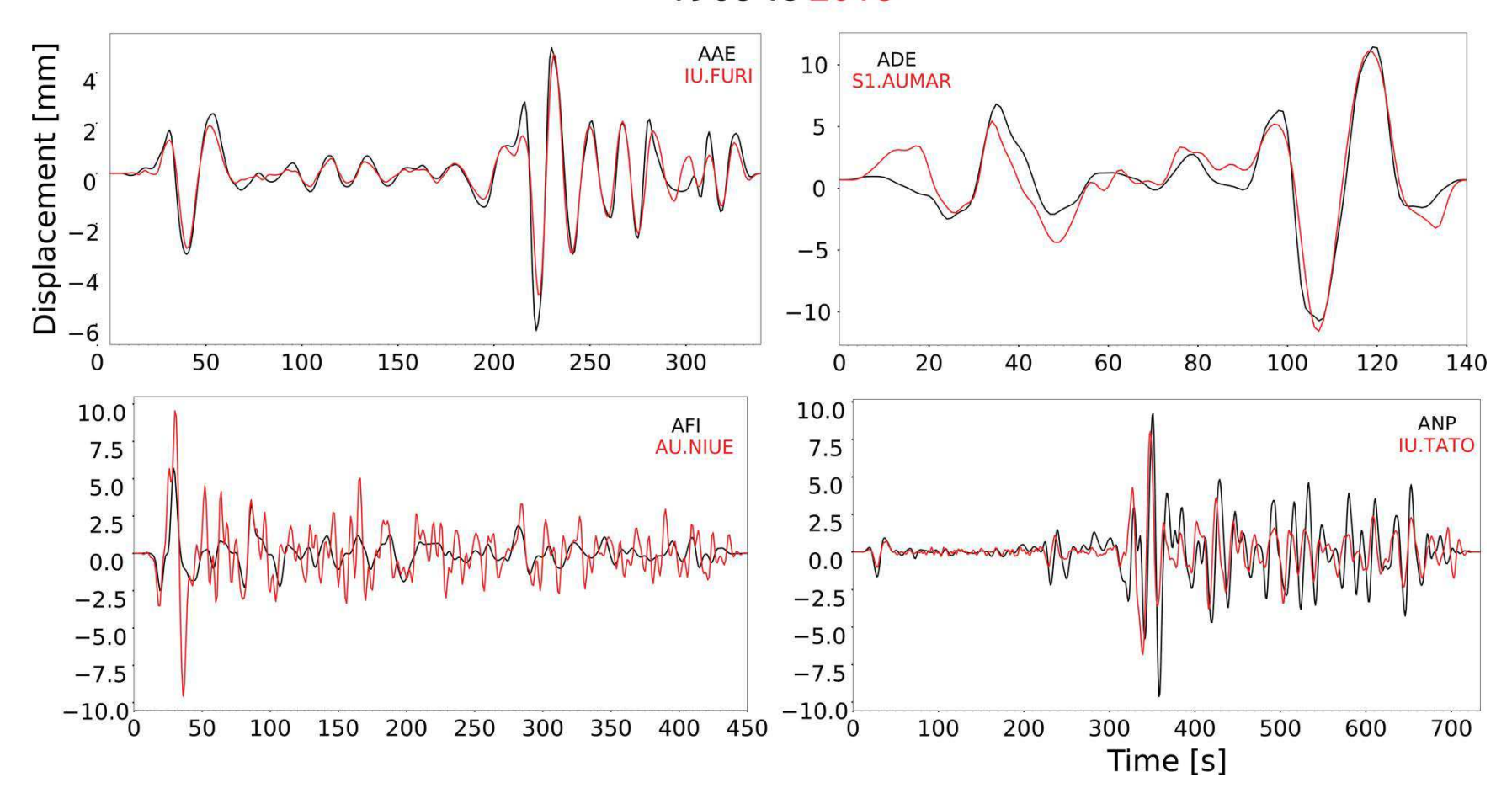


Figure S2. Waveform comparison between the 1968 earthquake (black) and the 2018 earthquake (red) for all stations where data was available. The traces are bandpass filtered between 100 and 5 s using a two-pass filter with 4 corners.

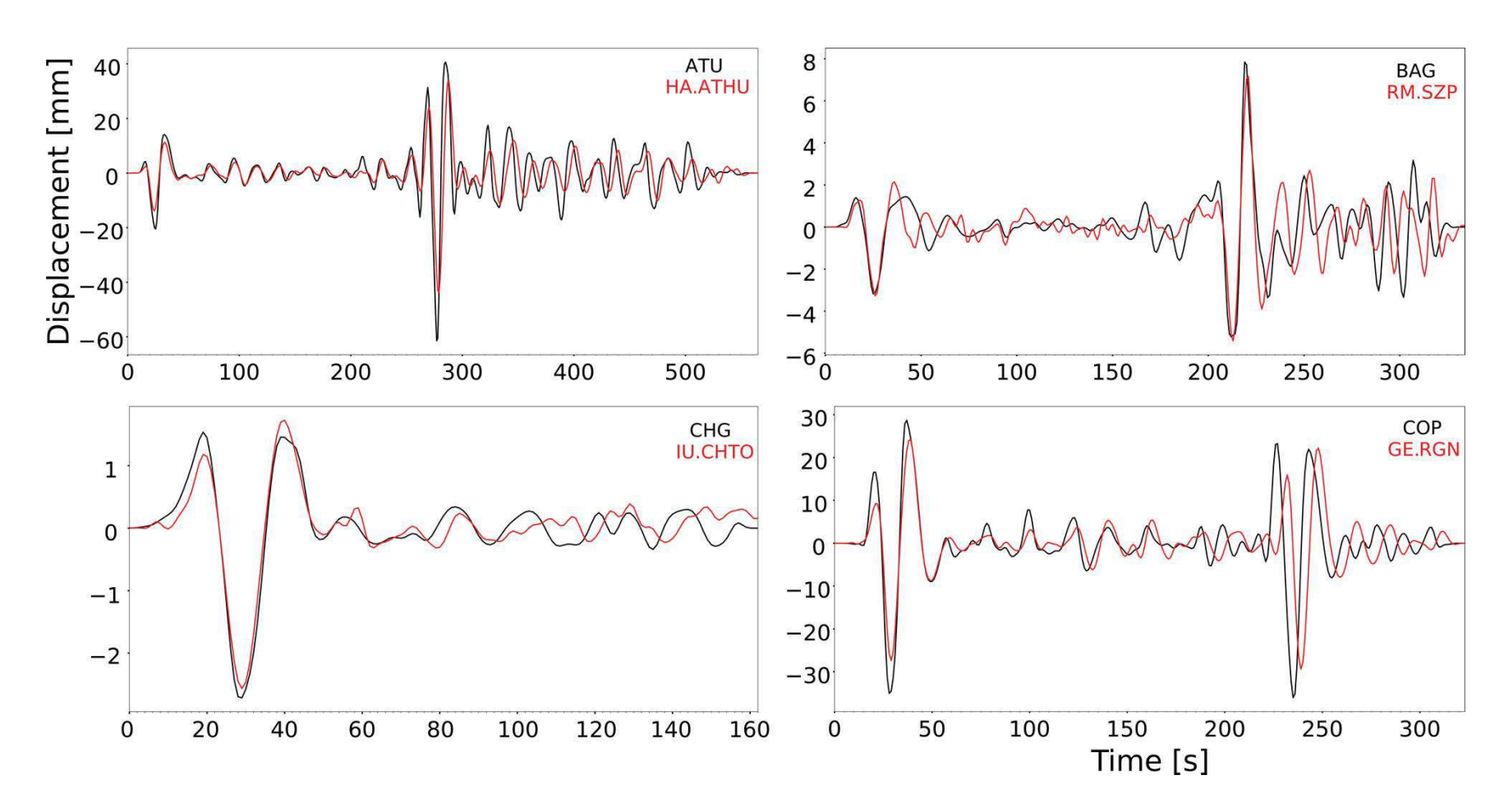


Figure S2. Continued.

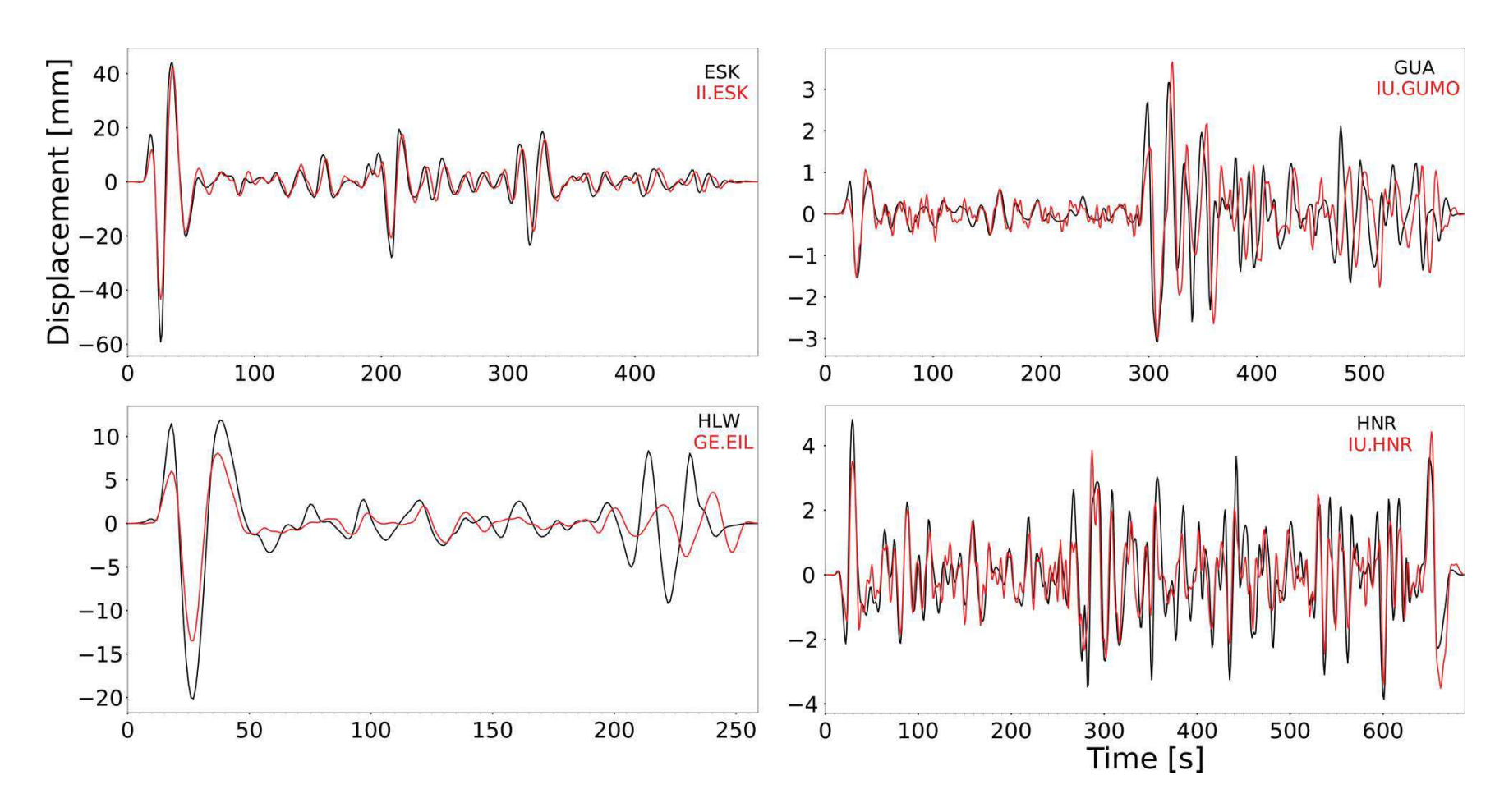


Figure S2. Continued.

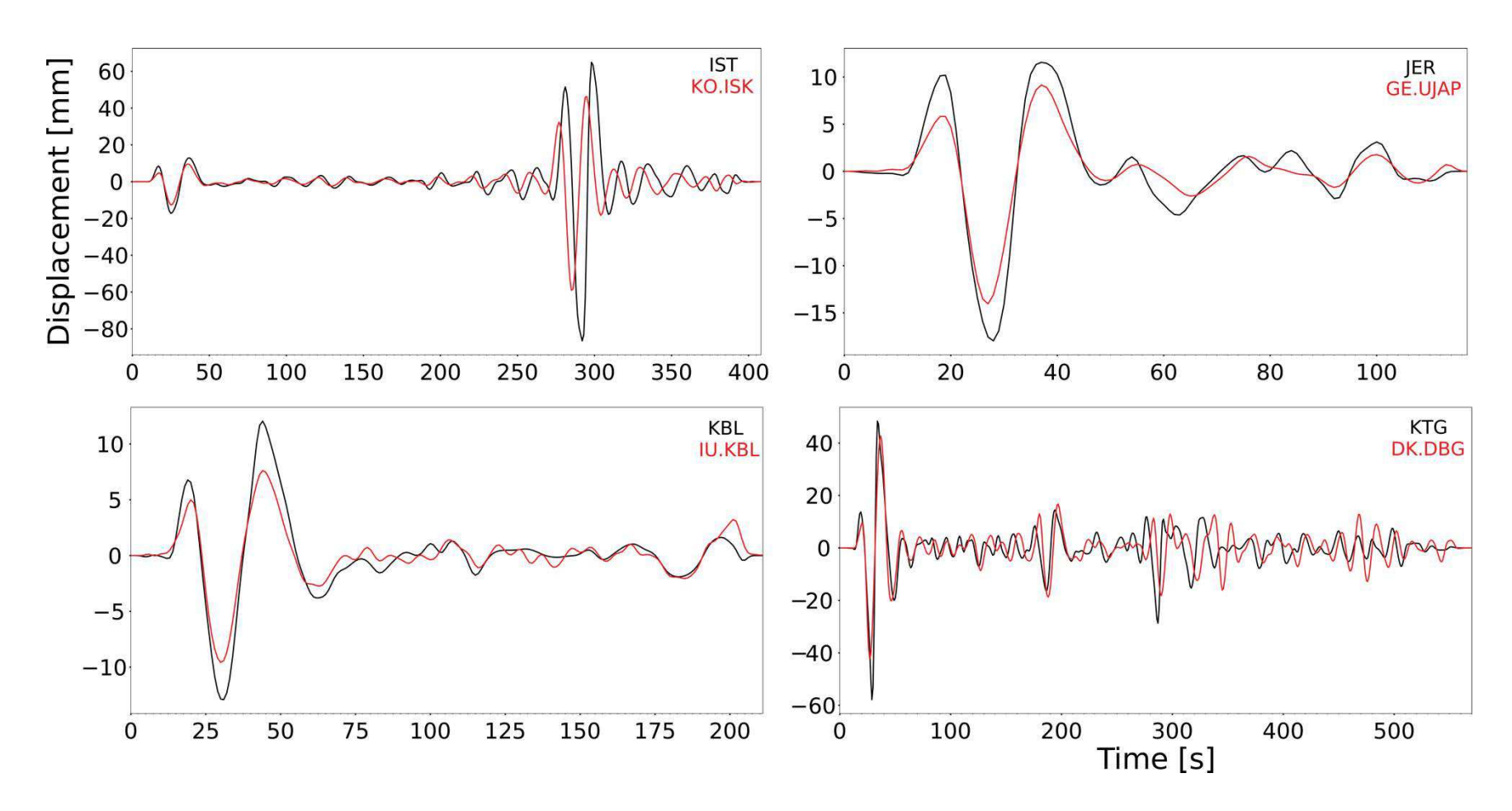


Figure S2. Continued.

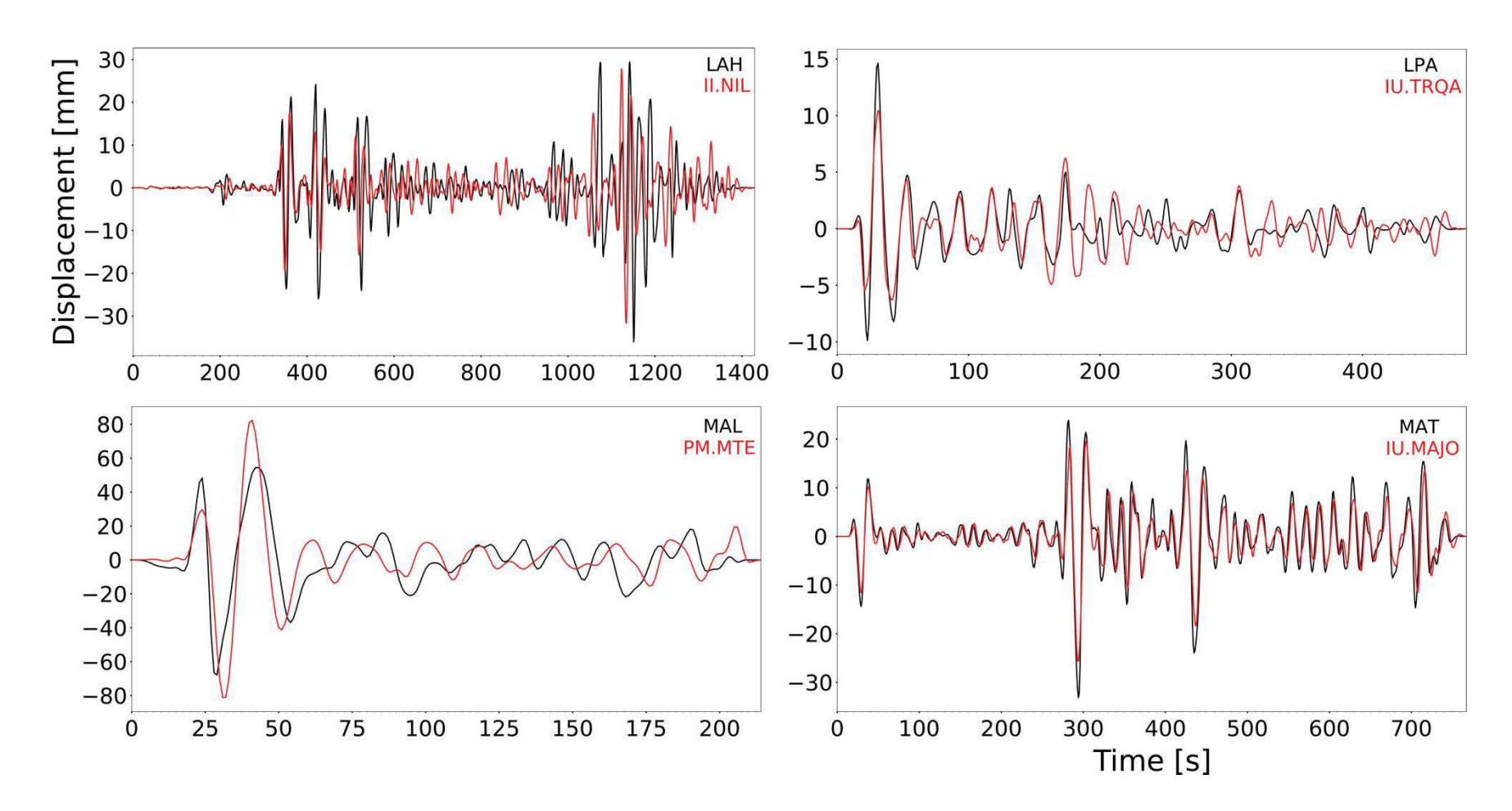


Figure S2. Continued.

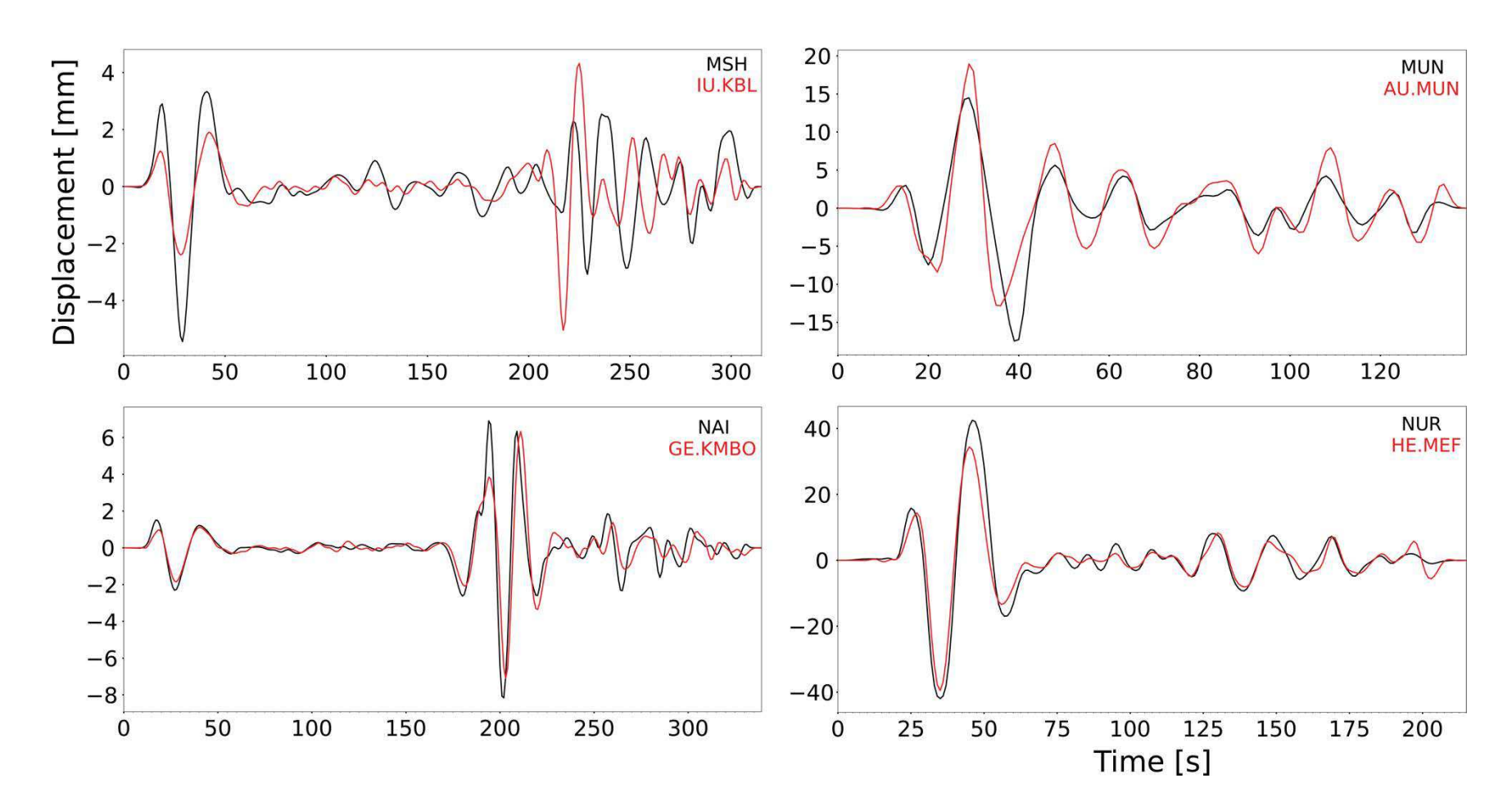


Figure S2. Continued.

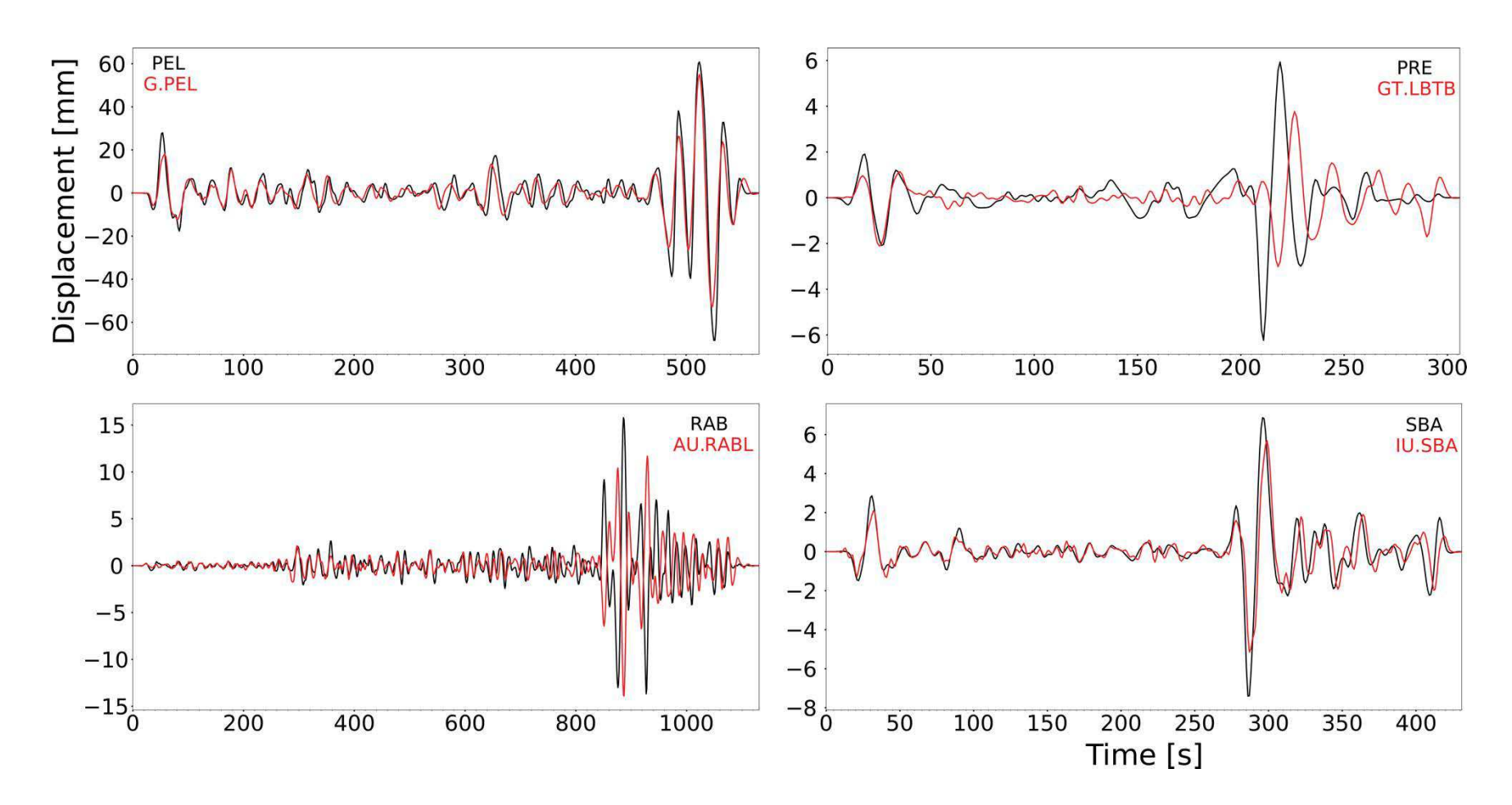


Figure S2. Continued.

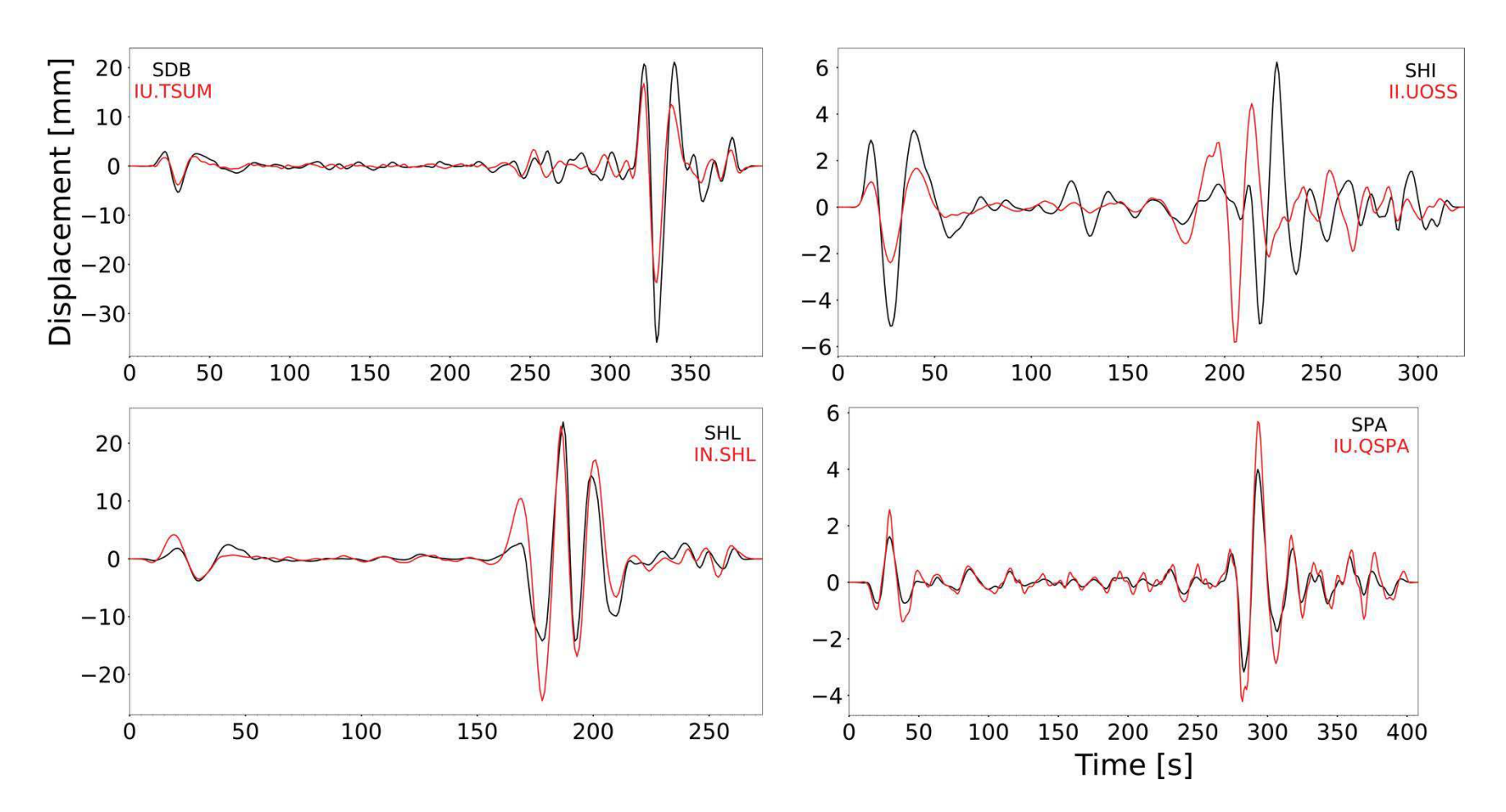


Figure S2. Continued.

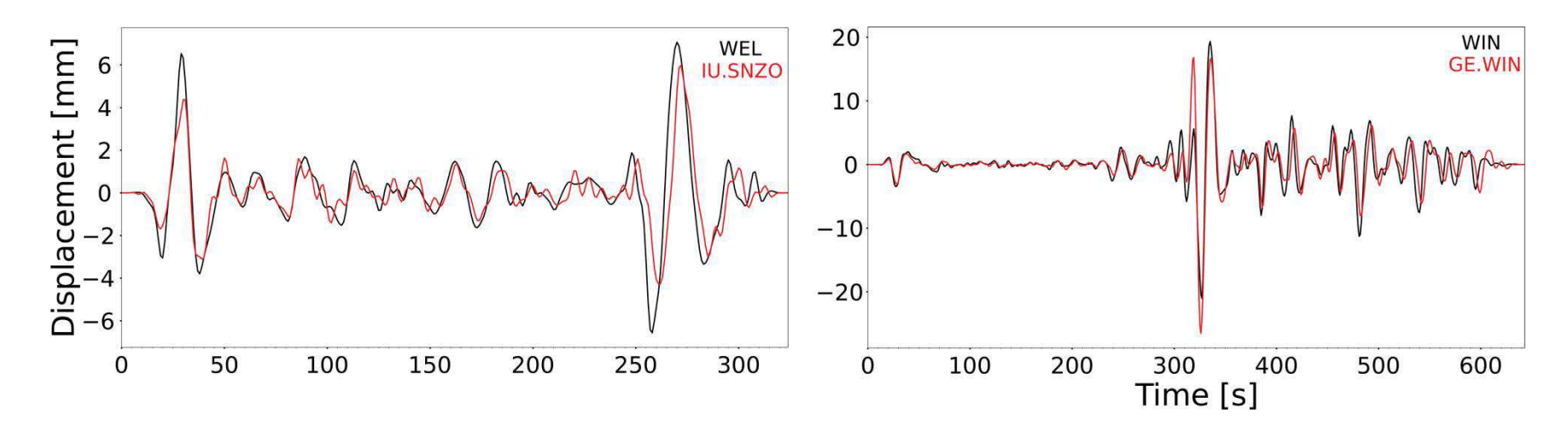


Figure S2. Continued.

WWSSN code	WWSSN location	Lat wwssn [°]	Lon wwssn [°]	Δ wwssn [°]	BB code	BB location	Lat BB [°]	Lon BB [°]	Δ вв [°]	Station distance [km]	WWSSN MAG	Length of trace [s]	150 s CC	300 s CC	Full CC
AFI	Afiamalu, Samoa Islands	-13.91	-171.78	80.58	AFI	Afiamalu, Samoa Islands	-13.91	-171.78	80.58	0	750	614	0.81	0.86	0.78
COP	Copenhagen, Denmark	55.68	12.43	86.87	COP	Copenhagen, Denmark	55.68	12.43	86.87	0	750	340	0.96	0.93	0.93
ESK	Eskdalemuir, Scotland	55.32	-3.21	78.56	ESK	Eskdalemuir, Scotland	55.32	-3.21	78.56	0	750	721	0.97	0.96	0.85
HNR	Honiara, Solomon Islands	-9.43	159.95	105.97	HNR	Honiara, Solomon Islands	-9.43	159.95	105.97	0	1500	444	0.58	0.76	0.70
KEV	Kevo, Finland	69.76	27.01	85.67	KEV	Kevo, Finland	69.76	27.01	85.67	0	1500	145	0.96	N/A	0.96
KIP	Kipapa, Hawaii	21.42	-158.01	58.65	KIP	Kipapa, Hawaii	21.42	-158.01	58.65	0	750	690	0.65	0.56	0.70
LPA	La Plata, Argentina	-34.91	-57.93	62.34	TRQA	Tornquist, Argentina	-38.06	-61.98	62.68	503	750	564	0.87	0.69	0.62
NOR	Nord, Greenland	81.6	-16.68	72.73	NOR	Nord, Greenland	81.6	-16.68	72.73	0	750	338	0.93	0.95	0.94
NUR	Nurmijärvi, Finland	60.51	24.65	90.18	KONO	Kongsberg, Norway	59.65	9.60	83.95	838	1500	261	0.88	N/A	0.80
SBA	Scott Base, Antarctica	-77.85	166.76	107.04	SBA	Scott Base, Antarctica	-77.85	166.76	107.04	0	750	693	0.83	0.92	0.77
SJG	San Juan, Puerto Rico	18.11	-66.15	28.61	SJG	San Juan, Puerto Rico	18.11	-66.15	28.61	0	750	109	0.64	N/A	0.71
SOM	Sombrero, Chile	-52.78	-69.24	72.45	GO10	Punta Arenas, Chile	-53.16	-71.10	72.31	128	375	76	0.86	N/A	0.90
WEL	Wellington, New Zealand	-41.29	174.77	99.83	SNZO	South Karori, New Zealand	-41.31	174.7	99.89	5	750	645	0.94	0.96	0.94

Table S2. Summary of data and results for the comparison between the 1965 earthquake recorded by the WWSSN network and the 2020 earthquake recorded in broad-band stations. Notation: Δ=Epicentral distance; **BB**=Broad-band; **CC**=Cross-correlation.

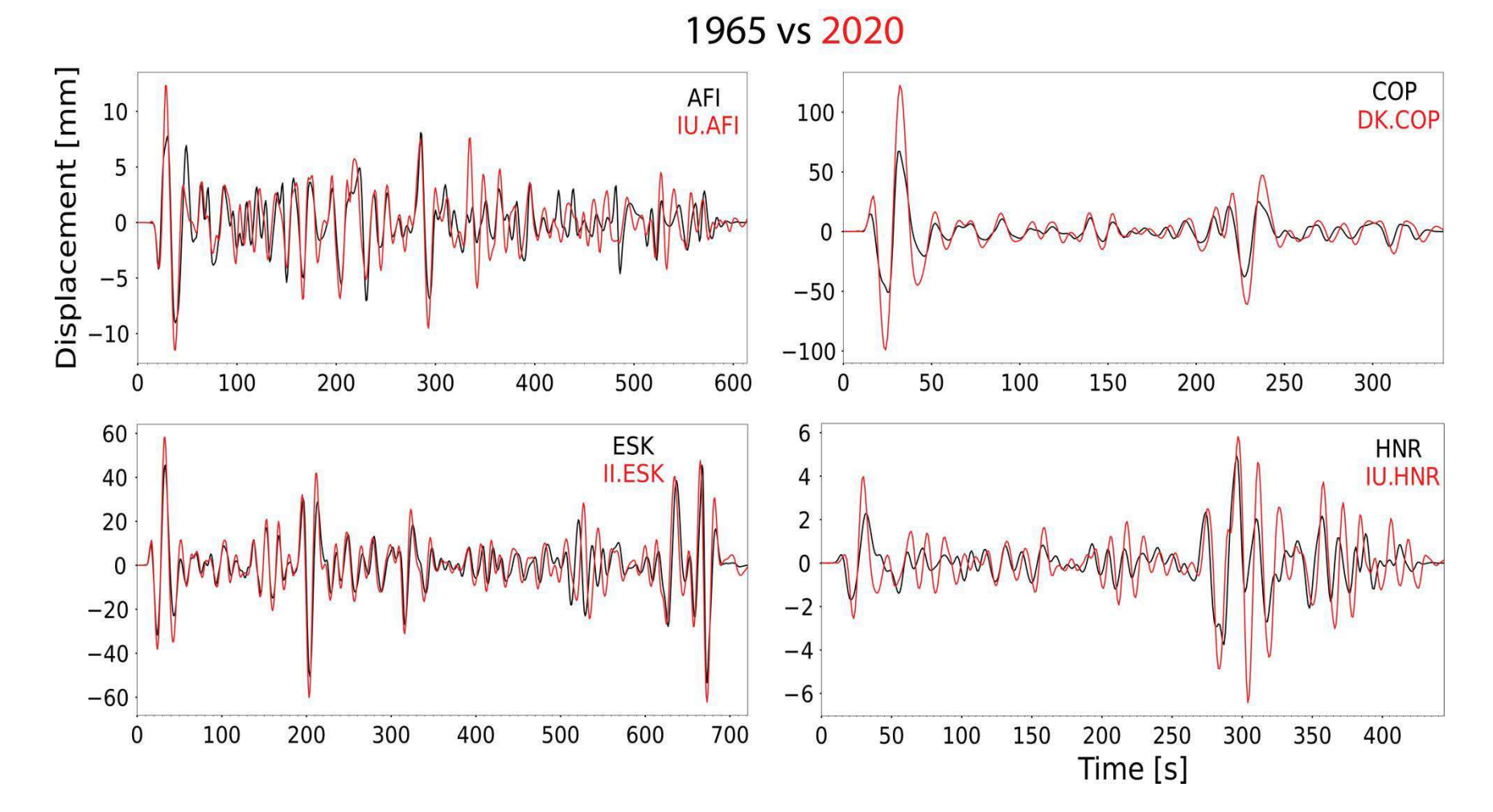


Figure S3. Waveform comparison between the 1965 earthquake (black) and the 2020 earthquake (red) for all stations where data was available.

The traces are bandpass filtered between 100 and 5 s using a two-pass filter with 4 corners.

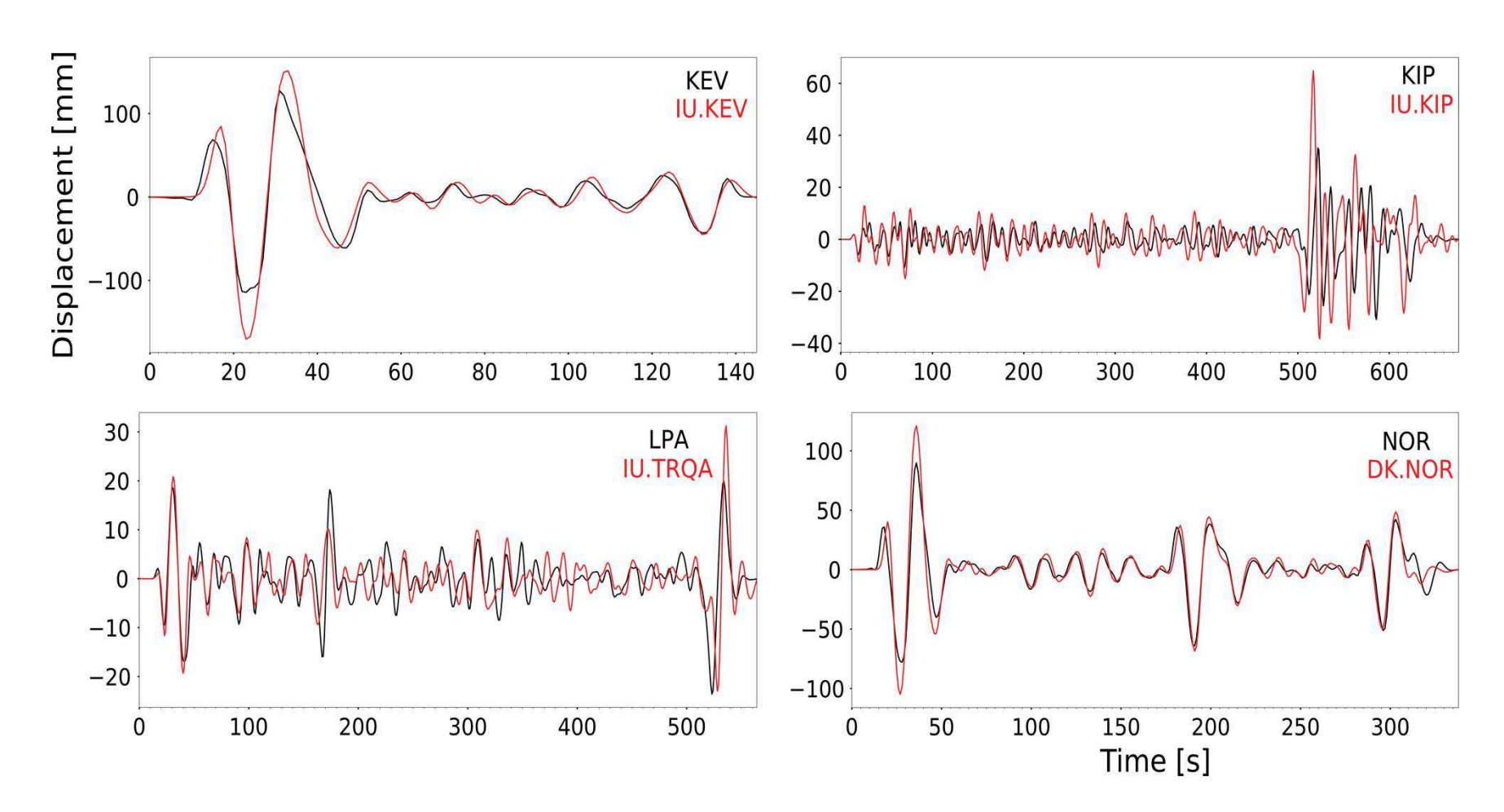


Figure S3. Continued.

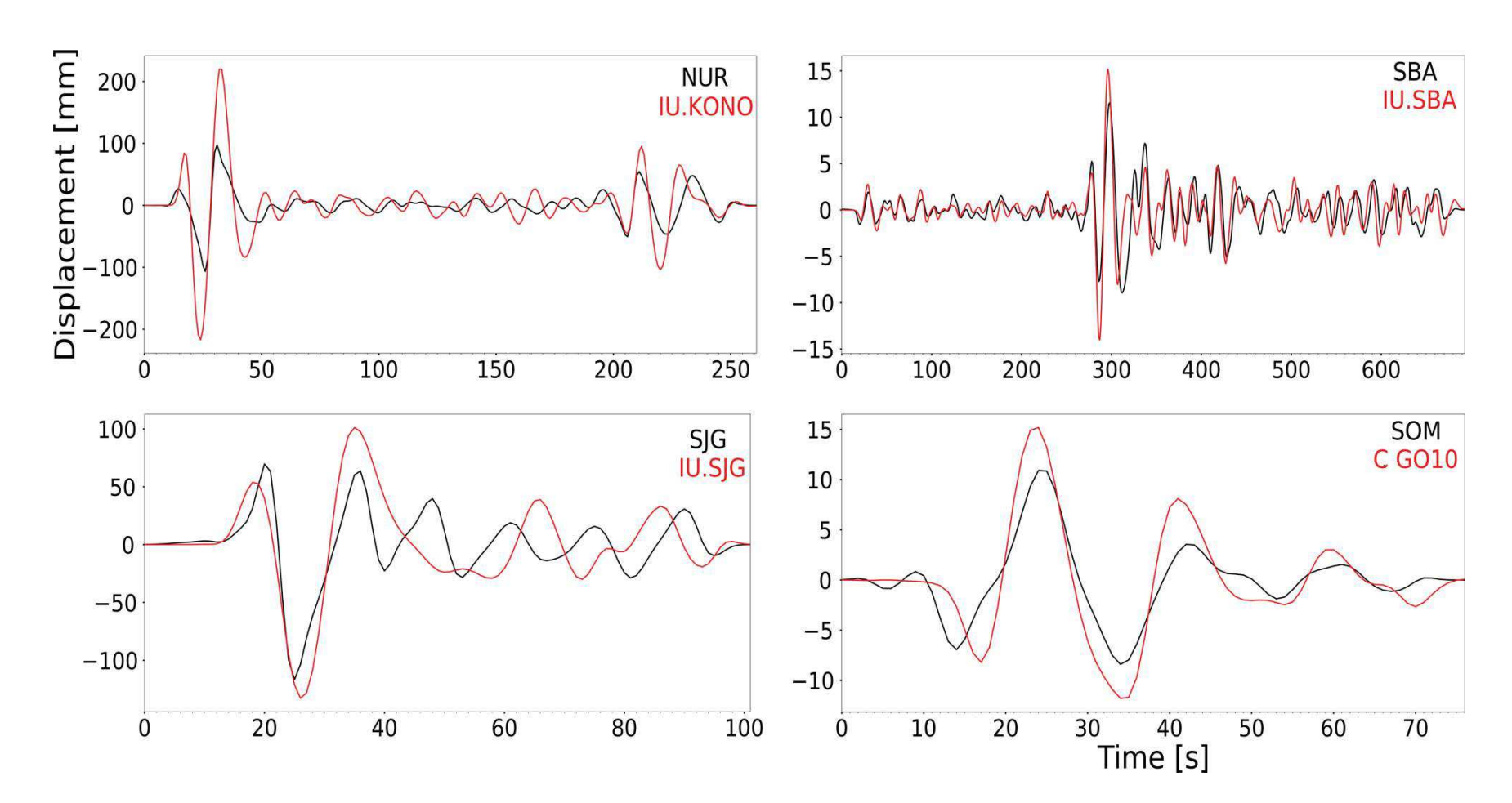


Figure S3. Continued.

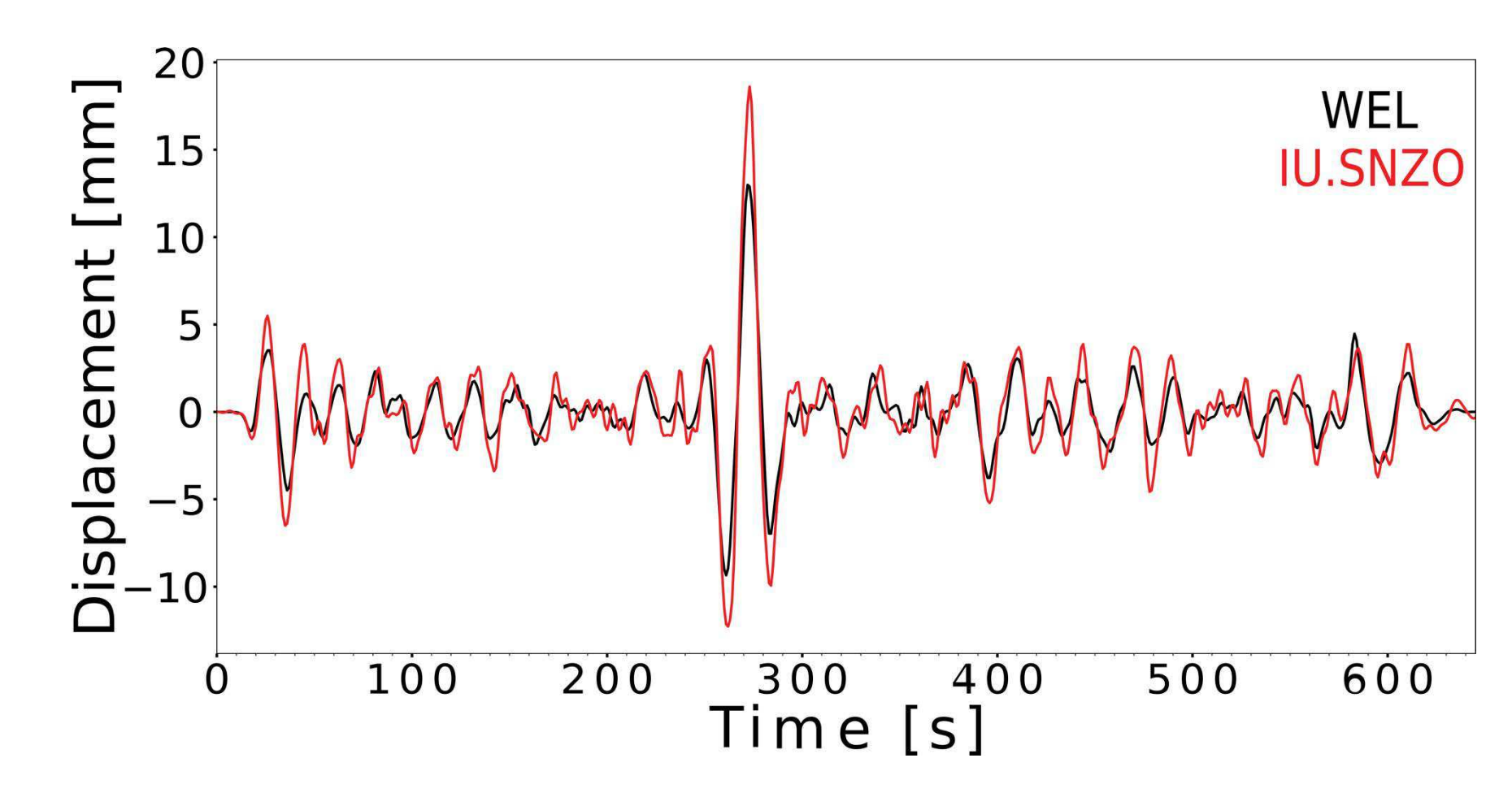


Figure S3. Continued.

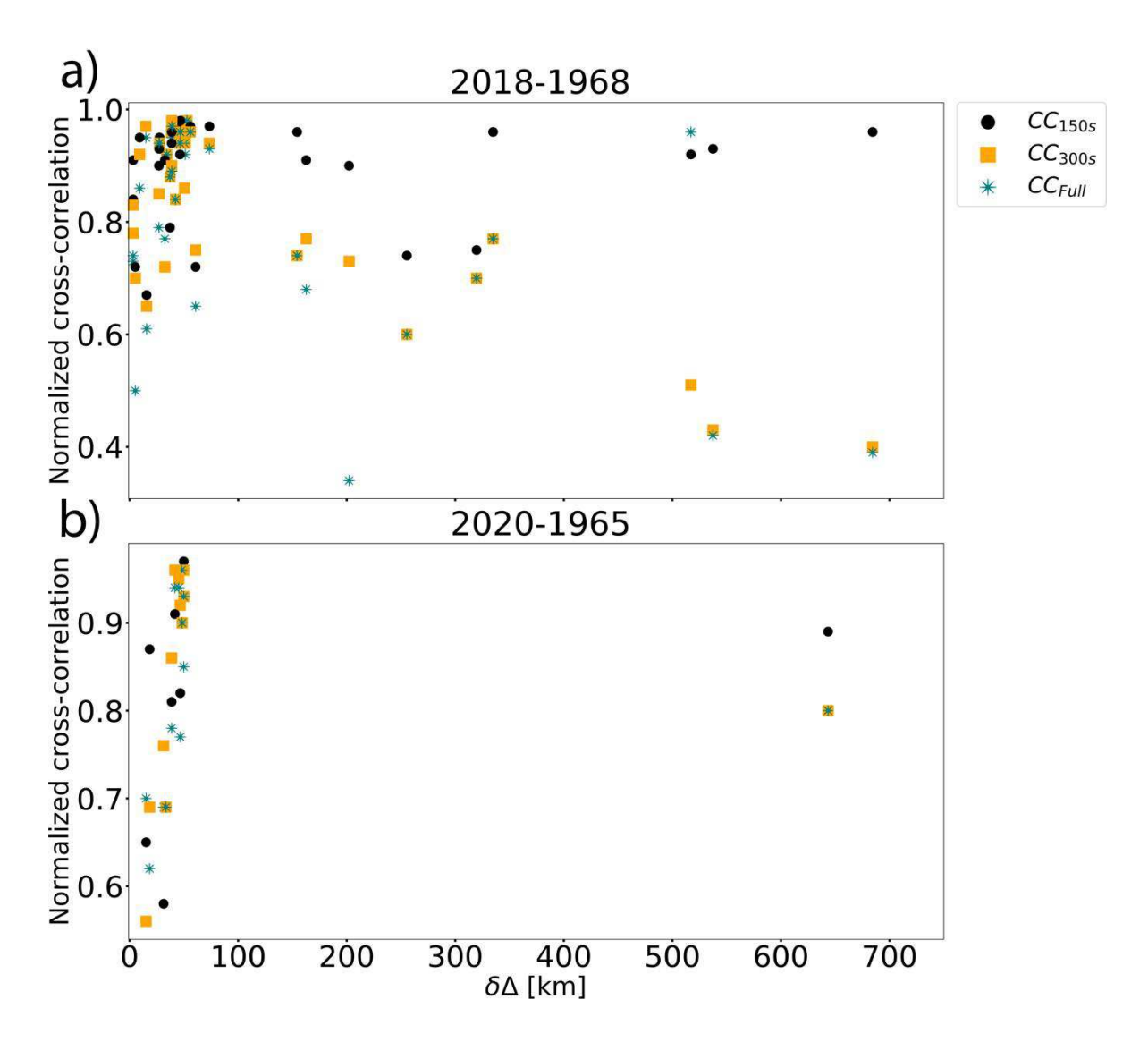


Figure S4. Normalized waveform cross correlations for (a) the 2018 and 1968 and (b) the 2020 and 1965 Oaxaca events plotted versus difference in epicentral distance between stations used in the comparisons. Results are color-coded by duration of the time windows used; 150 s, 300 s, and the total length available.

Date	Lat. [°]	Lon. [°]	$M_{\rm w}$	# Stations Used
06-23-2020	15.886	96.008	7.4	13
02-16-2018	16.386	97.979	7.2	34
03-20-2012	16.493	98.231	7.4	9-18
02-25-1996	15.978	98.070	7.0	7-14
09-14-1995	16.779	98.597	7.4	7-12
08-02-1968	16.519	97.739	7.3	34
08-23-1965	16.081	95.867	7.4	13

Table S3. USGS-NEIC Locations of all Oaxaca Events Analyzed

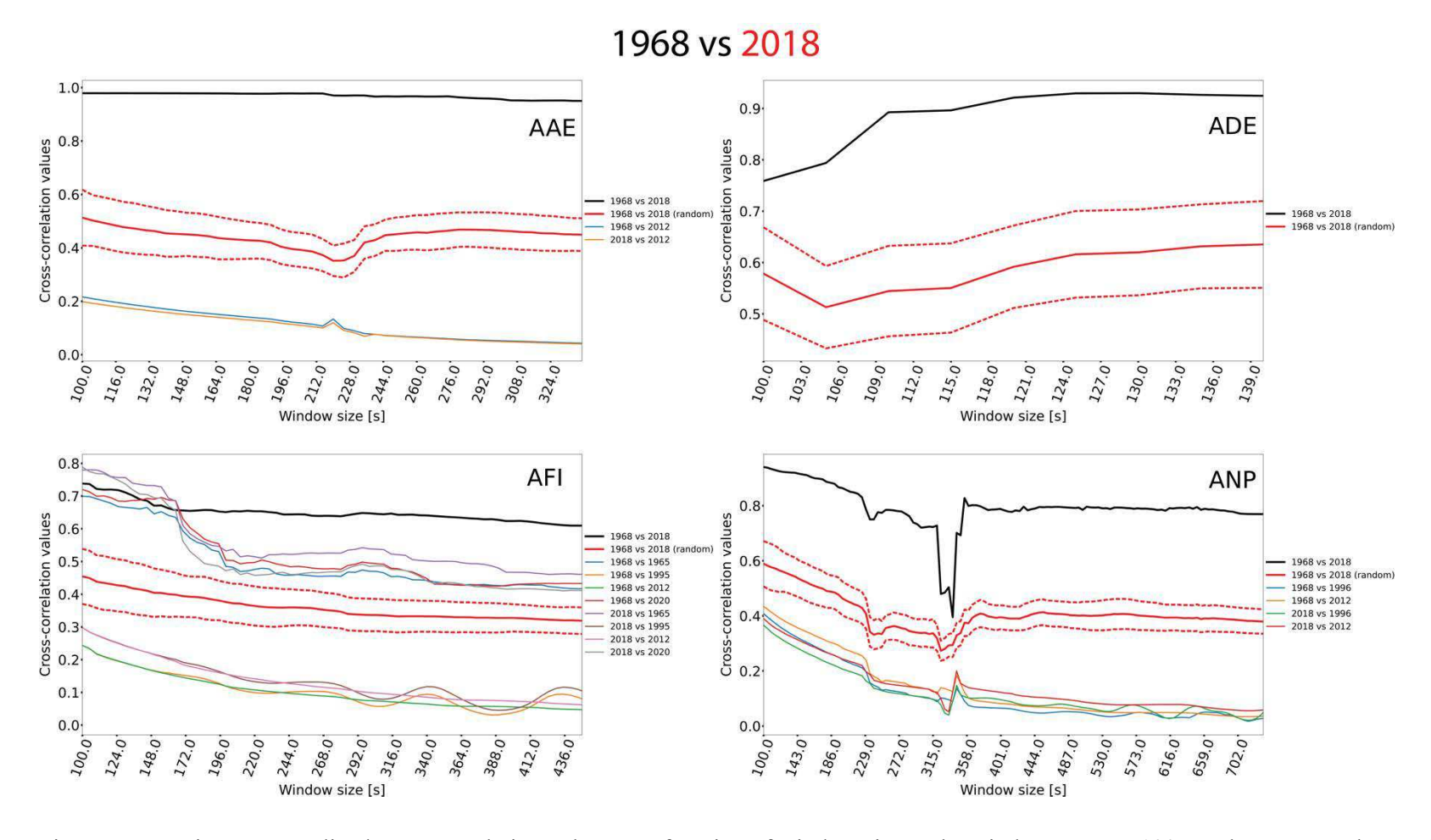


Figure S5. Maximum normalized cross correlation values as a function of window sizes. The windows start at 100 s and span up to the maximum length of the digitized records in 5 s increments. The thick black line represents the cross correlations for the 1965 and 2020 La Crucecita earthquakes, the thick red line is the mean stack of 100 realizations of cross correlations between the data for the 1965 event with random phase data from the 2020 earthquake and the dashed red lines show one standard deviation, and the colored lines represent the comparison for 1965 and 2020 with earthquakes from 1968, 1995, 1996, 2012 and 2018. In almost all cases the black curve remains above all other curves.

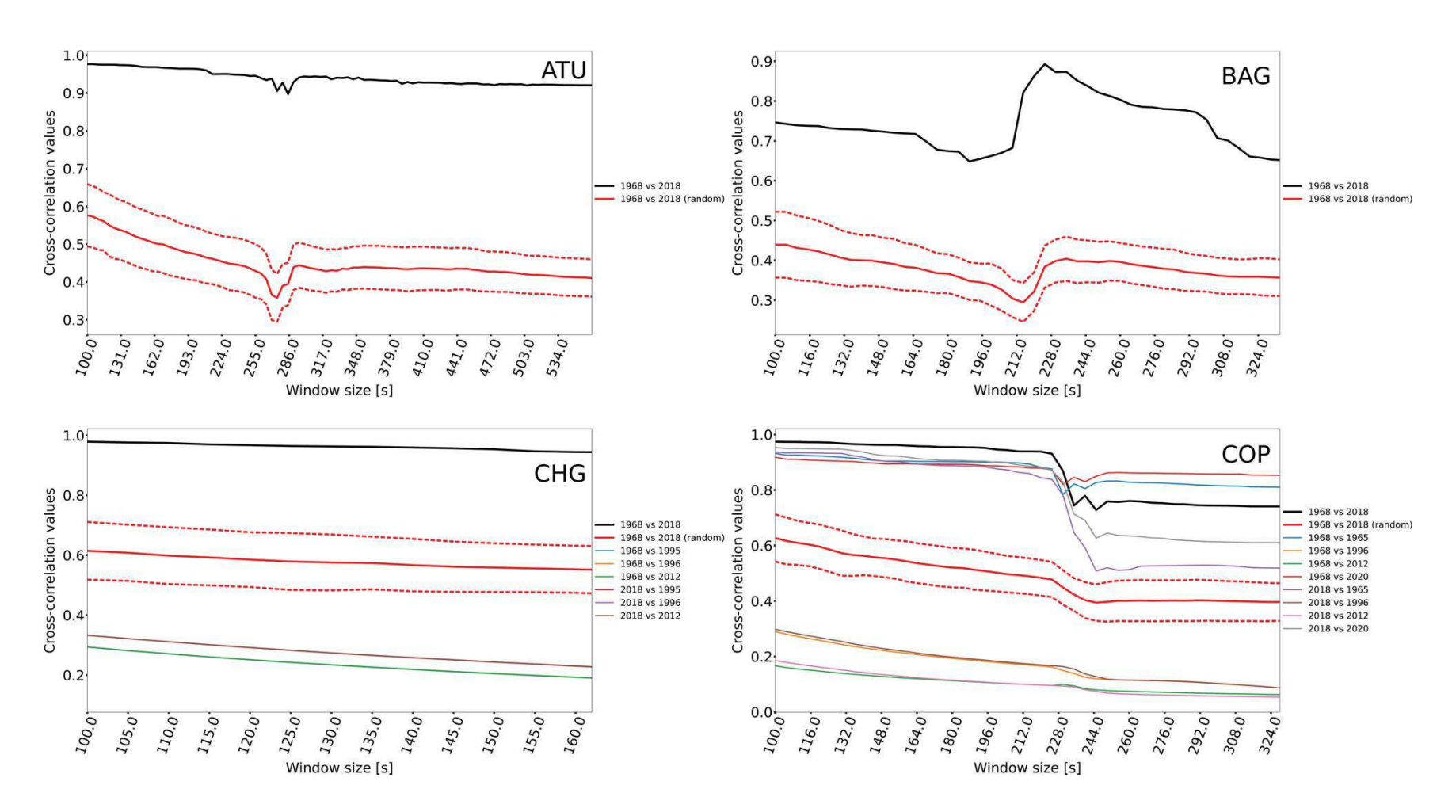


Figure S5. Continued.

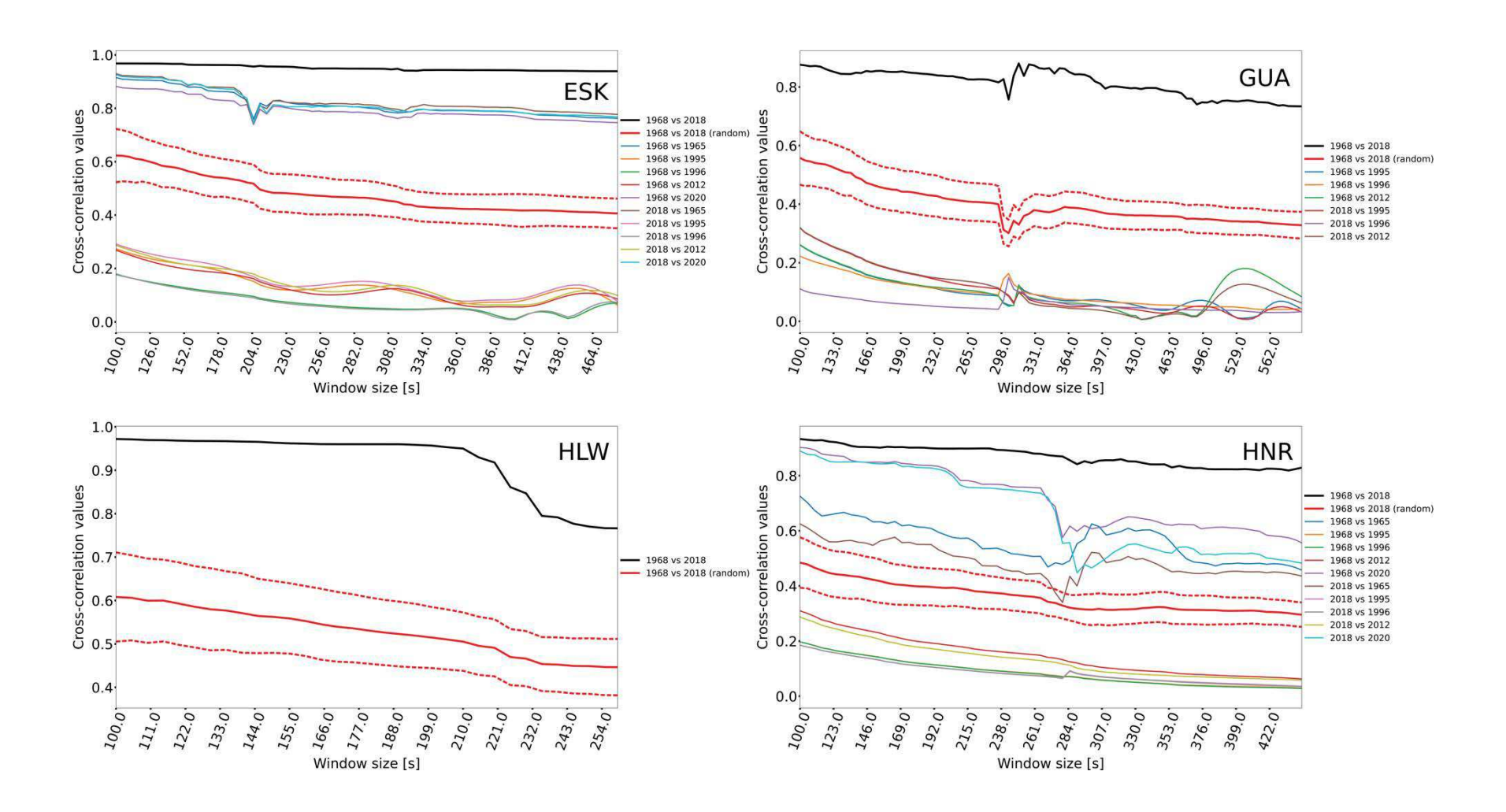


Figure S5. Continued.

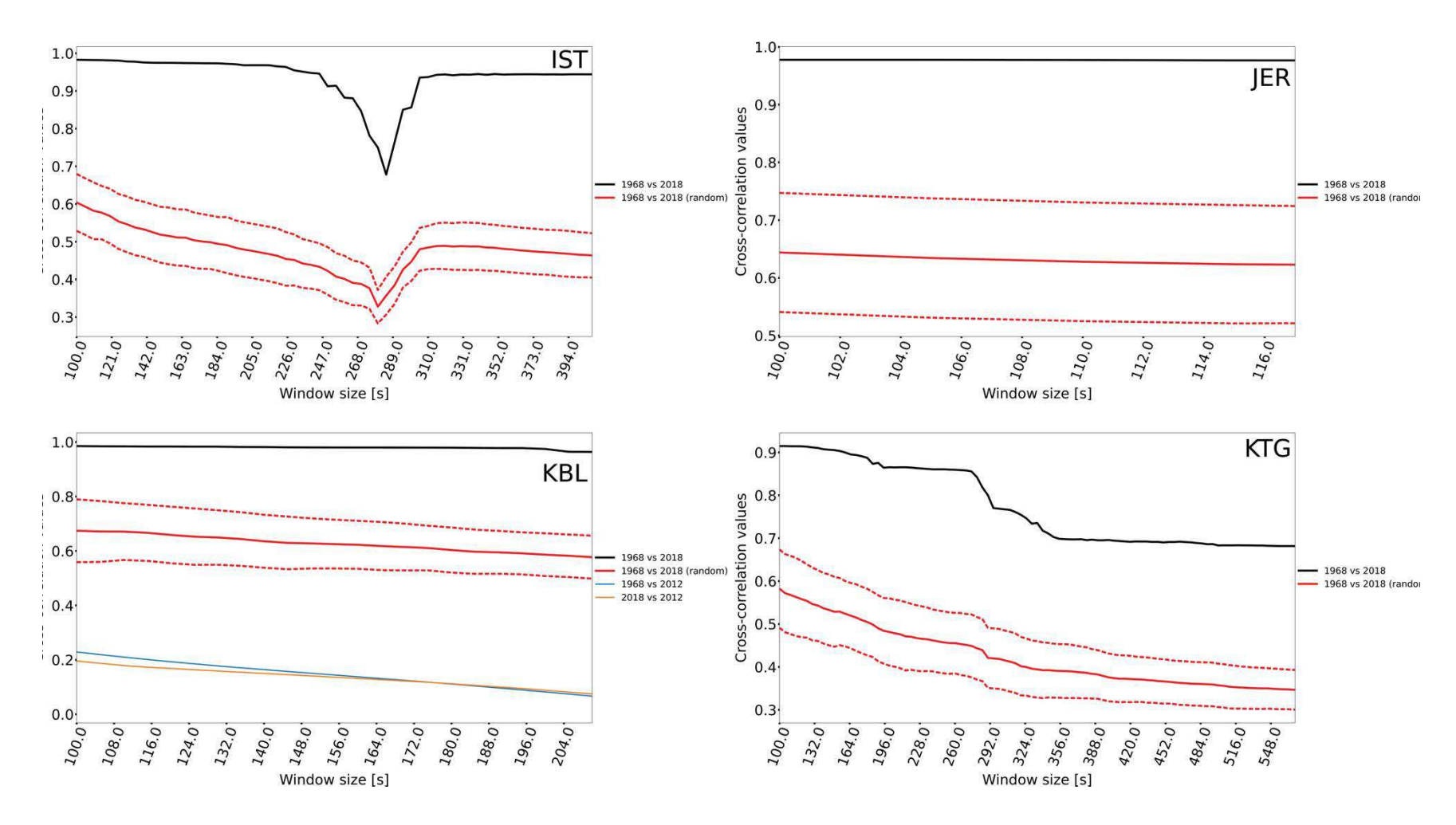


Figure S5. Continued.

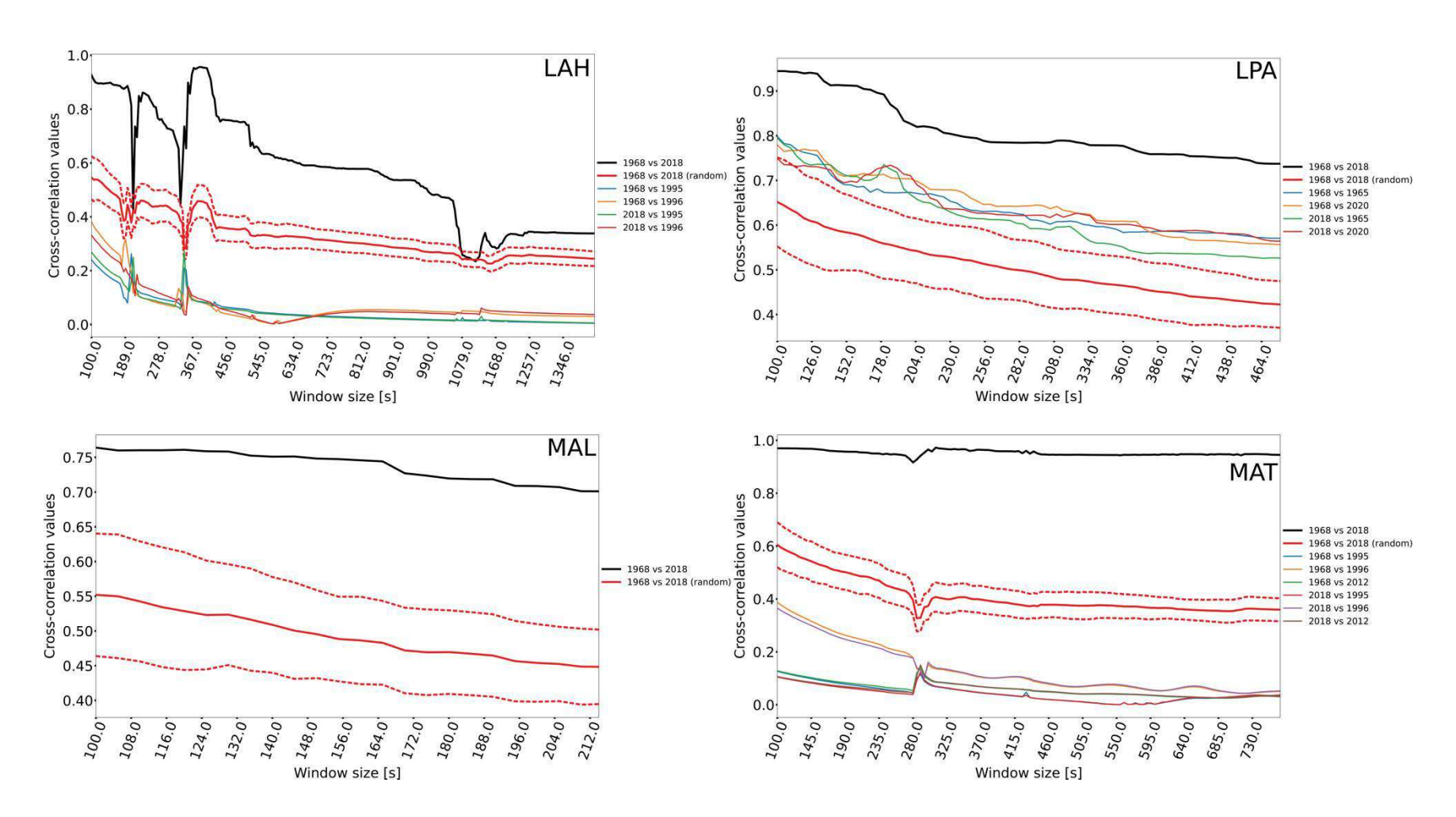


Figure S5. Continued.

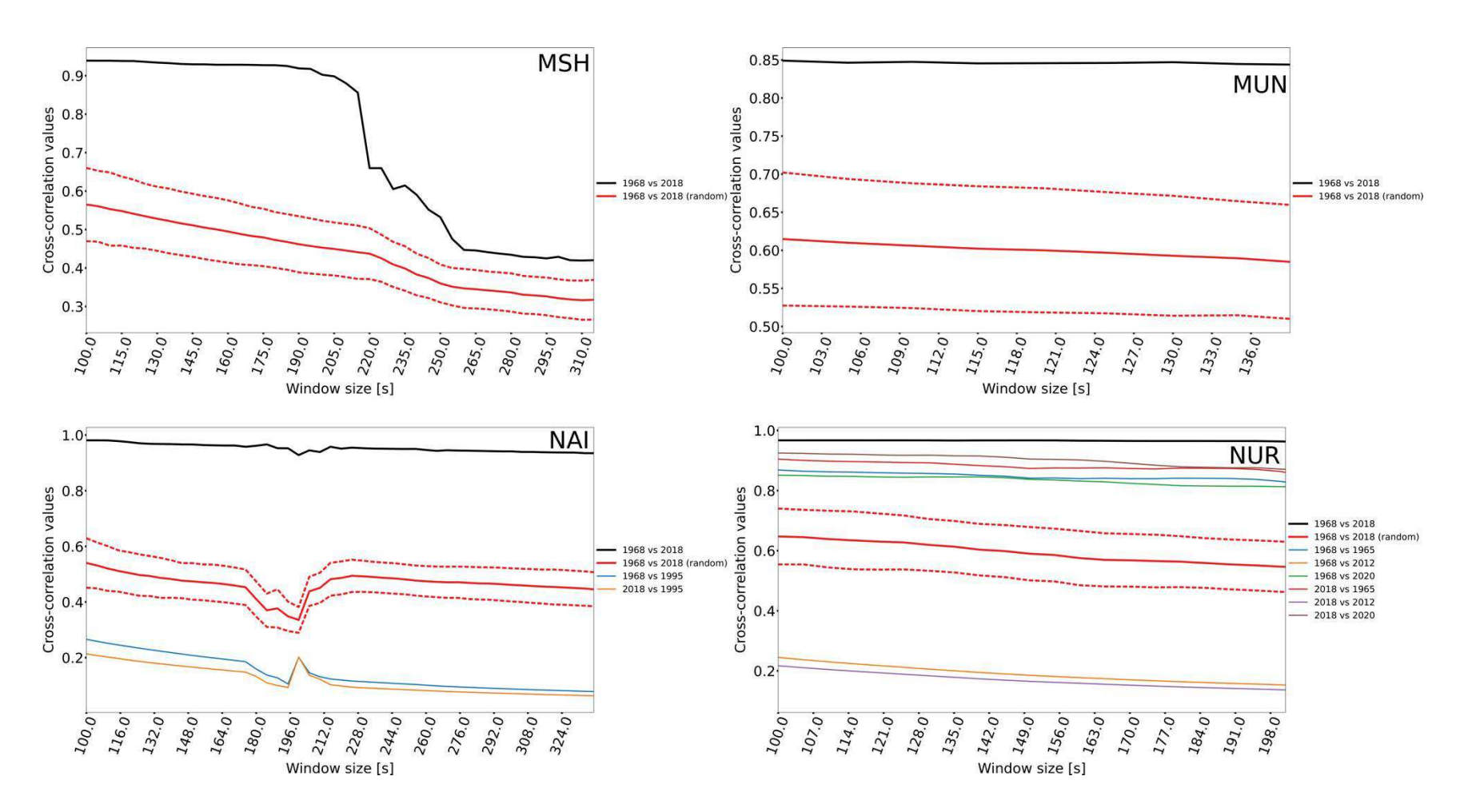


Figure S5. Continued.

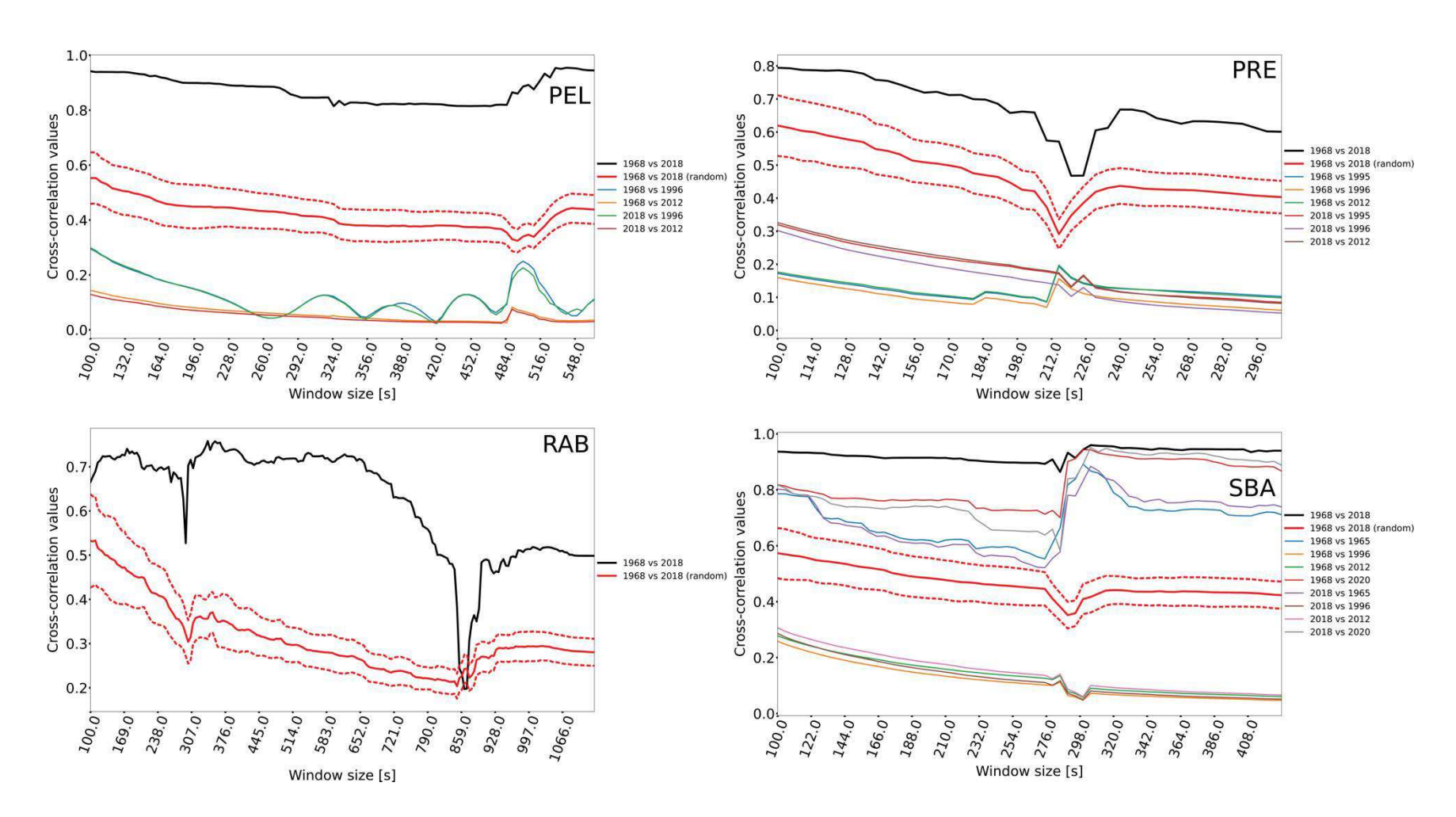


Figure S5. Continued.

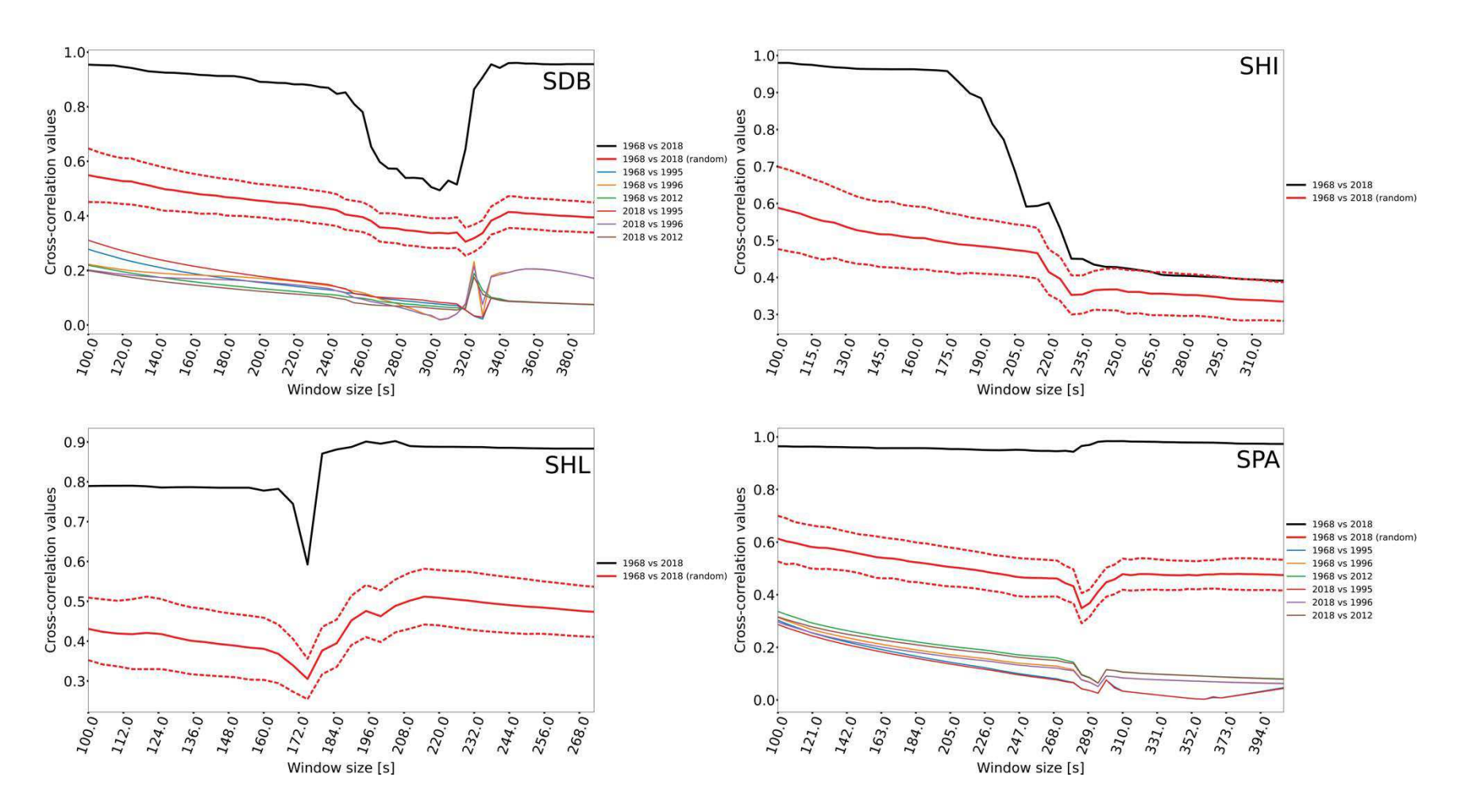


Figure S5. Continued.

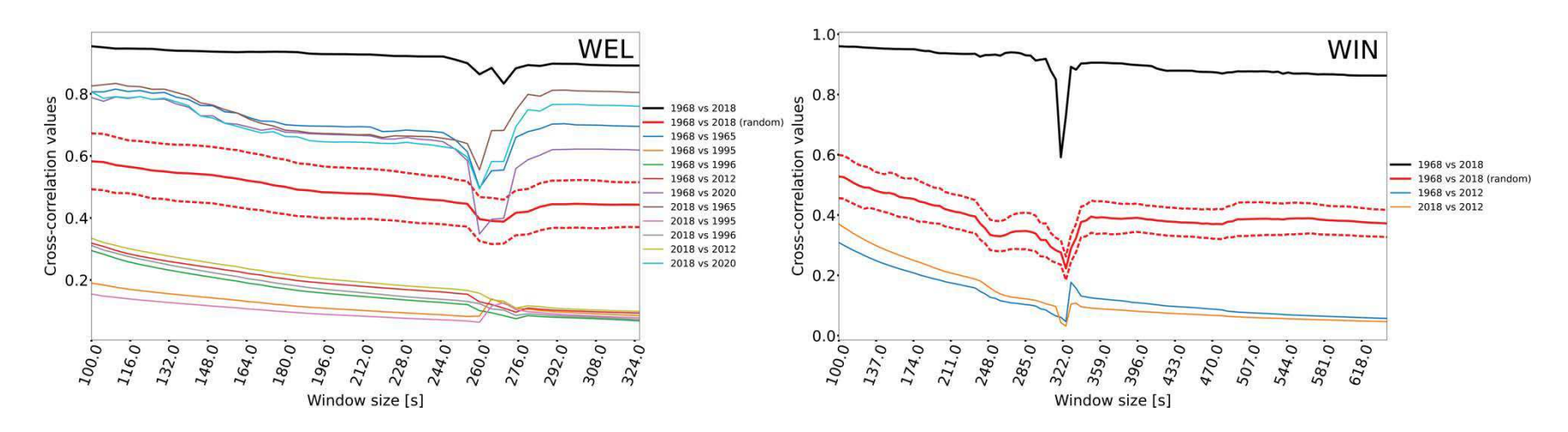


Figure S5. Continued.

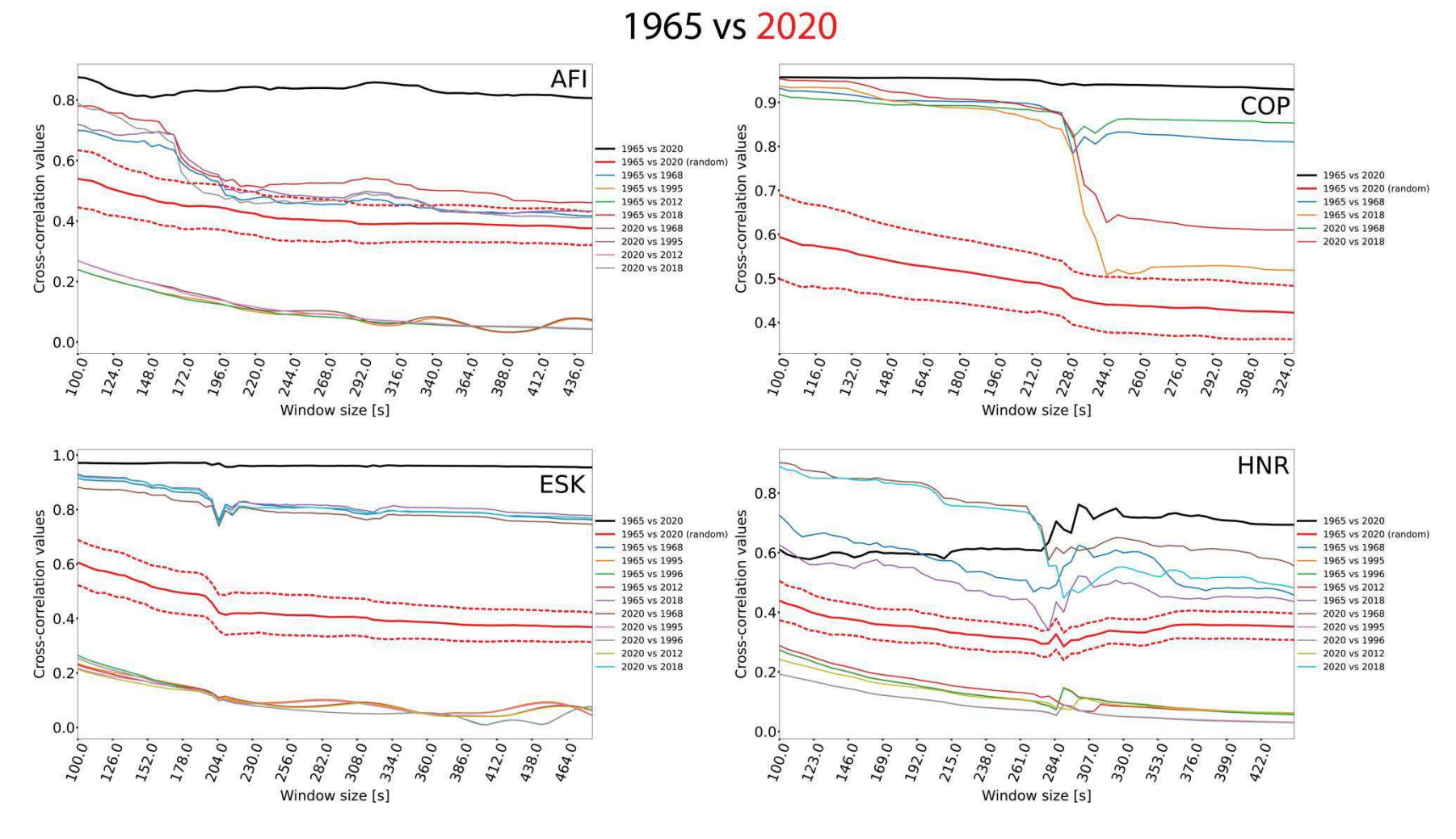


Figure S6. Maximum cross correlation values for different window sizes. The windows start at 100 s and span up to the maximum length of the digitized records in 5 s increments. The thick black line represents the cross-correlations for the 1965 and 2020 La Crucecita earthquakes, the thick red line is the mean stack of 100 realizations of cross-correlations between the data for the 1965 event with random phase data from the 2020 earthquake and the dashed red lines show one standard deviation, and the colored lines represent the comparison for 1965 and 2020 with earthquakes from 1968, 1995, 1996, 2012 and 2018. In almost all cases the black curve remains above all other curves.

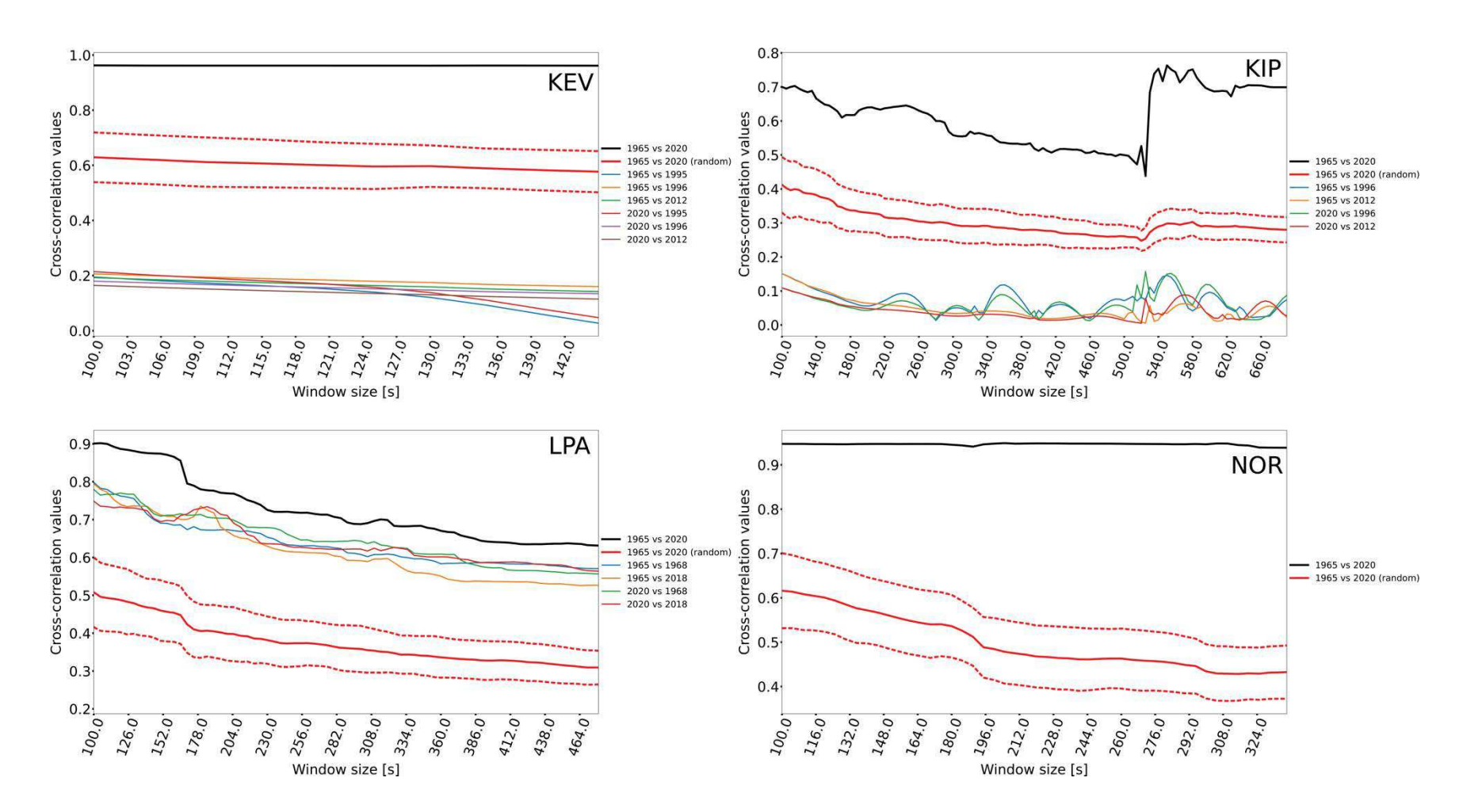


Figure S6. Continued.

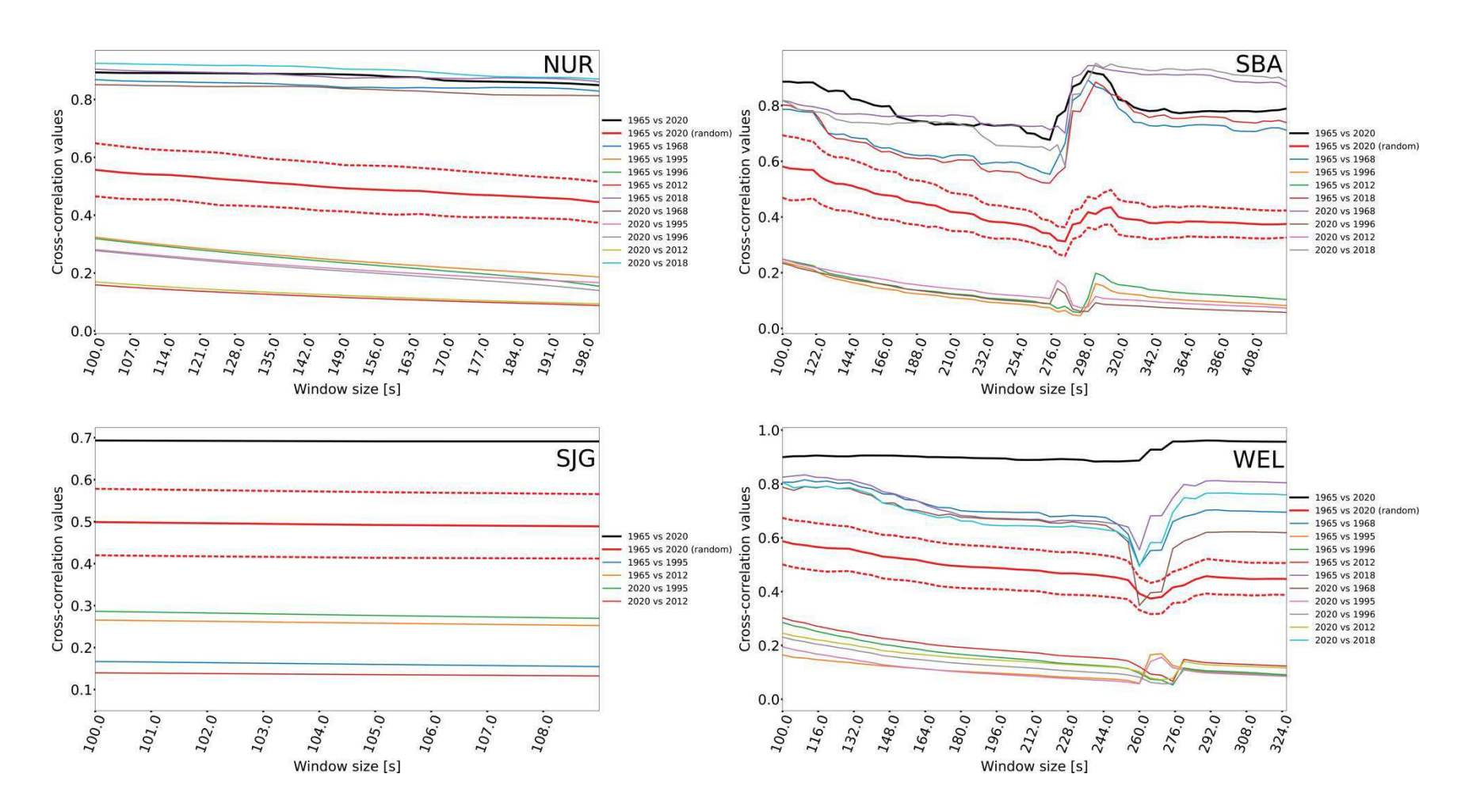


Figure S6. Continued.